Wheel–rail contact simulation with lookup tables and KEC profiles: a comparative study

Escalona José Luis, Yu Xinxin, Aceituno Javier F.

DOI: 10.1007/s11044-020-09773-7

Wheel-rail contact simulation with lookup tables and KEC profiles: A comparative study

José L. Escalona[a,*], Xinxin Yu[b], Javier F. Aceituno[c]

[a] *Dept. of Mechanical and Manufacturing Engineering, University of Seville (Spain)*

[b] *Dept. of Mechanical Engineering, LUT University (Finland)*

[c] *Dept. of Mechanical and Mining Engineering, University of Jaén (Spain)*

Abstract

This paper describes and compares the use and limitations of two constraint-based formulations for the wheel-rail contact simulation in multibody dynamics; (1) the use of contact lookup tables and (2) the Knife-edge Equivalent Contact constraint method (KEC-method). Both formulations are presented and an accurate procedure to interpolate within the data in the lookup table is also described. Since the wheel-rail constraint contact approach finds difficulties at simultaneous tread and flange contact scenarios, the lookup table method is implemented with a penetration-based elastic contact model for the flange, turning the method into a hybrid (constant in the tread and elastic in the flange) approach. To deal with the 2-point contact scenario in the KEC-method, a regularisation of the tread-flange transition allows the use of the constraint approach in the tread and also in the flange. To show the applicability and limitations of both methods, they are studied and compared with special emphasis in the calculation of normal and tangential contact forces. Numerical results are based on the simulation of a two-wheeled bogie vehicle in different case studies that consider irregular tracks and two wheel-rail profiles combination: profiles that do not show two-point wheel-rail contacts and profiles that do show two-point wheel-rail contacts. Although results show a good agreement between both approaches, the use of the KEC-method is more extensive since it allows to reproduce the wheel-climbing scenario that cannot be simulated with the lookup table method with the hybrid contact approach. It is concluded that simulations with this later method may not be in the safe side.

Keywords: Contact lookup table, KEC-method , Interpolation, Wheel-rail contact, Wheel-climbing

Nomenclature

$\bar{\mathbf{r}}^{lir}$, $\bar{\mathbf{r}}^{rir}$ The relative position vector of the irregular rail centreline with respect to the ideal rail centreline.

*Corresponding author

Email addresses: escalona@us.es (José L. Escalona), xinxin.yu@lut.fi (Xinxin Yu), jaceitun@ujaen.es (Javier F. Aceituno)

$\bar{\mathbf{r}}^{lrp}$, $\bar{\mathbf{r}}^{rrp}$ The relative position vector of the ideal rail centreline with respect to the the *track frame*.

$\bar{\mathbf{r}}_c^{wi}$, $\bar{\mathbf{r}}_c^{rp}$ The position vectors of contact points on the wheel and rail in *track frame*.

$\bar{\mathbf{t}}_{1,c}^{wi}$, $\bar{\mathbf{n}}_c^{rp}$ The unit-tangent vector and normal vector at the contact point in *track frame*.

β The orientation angle of the rail profiles

$\boldsymbol{\lambda}$ The array of Lagrange multipliers.

δ The linearised rotation angle due to the irregularity

δ^{wi}, $\dot{\delta}^{wi}$ The wheel-rail penetration at the flange contact and its time derivative.

$\hat{\mathbf{u}}_P^{rrp}$, $\hat{\mathbf{u}}_Q^{lrp}$ The position vector of points P and Q in the rail profiles.

$\hat{\mathbf{u}}_R^{wIi}$, $\hat{\mathbf{u}}_L^{wIi}$ The position of the points in the wheel surface with respect to the *wheelset intermediate frame*.

$\mathbf{A}^{t,lrp}$, $\mathbf{A}^{t,rrp}$ The rotation matrix from the *railhead frame* with respect to the *track frame*.

$\mathbf{A}^t$ The rotation matrix from the *track frame* to the *global frame*.

$\mathbf{A}^{wti,wi}$, $\mathbf{A}^{wti,wIi}$, $\mathbf{A}^{wIi,wi}$ The rotation matrices from *wheel frame* to the *wheelset track frame*, from *wheelset intermediate frame* to the *wheelset track frame* and from *wheel frame* to the *wheelset intermediate frame*.

$\mathbf{C}^{clt}$ The wheel-rail contact constraints constraint equations modelled with lookup tables.

$\mathbf{C}_{\mathbf{q}}^{clt}$, $\dot{\mathbf{C}}_{\mathbf{q}}^{clt}$ The Jacobian matrix and its time derivative of all wheel-rail contact constraints modelled with lookup tables.

$\mathbf{C}^{KEC}$ The contact constraint equations of a wheelset with KEC profiles.

$\mathbf{C}_{\mathbf{q}}^{KEC}$, $\dot{\mathbf{C}}_{\mathbf{q}}^{KEC}$ The Jacobian matrix and its time derivative of KEC contact constraint equations with respect to generalised coordinates $\mathbf{q}$.

$\mathbf{C}_{\mathbf{s}}^{KEC}$, $\dot{\mathbf{C}}_{\mathbf{s}}^{KEC}$ The Jacobian matrix and its time derivative of KEC contact constraint equations with respect to KEC surface parameters.

$\mathbf{n}_c^{rp}$ The normal vector to the rail surface at the contact point in *global frame*.

$\mathbf{Q}$ The force vectors of generalised applied forces and generalised quadratic-velocity inertia forces.

$\mathbf{Q}_{fla}^{nor}$, $\mathbf{Q}^{tang}$, $\mathbf{Q}_{tread}^{nor}$ The force vectors of generalised wheel-rail normal flange forces, generalised tangential tread and flange forces, and generalised normal forces at the wheel tread.

$\mathbf{R}^t$ The absolute position vector of an arbitrary point on the ideal track centreline with respect to a *global frame*.

$\mathbf{R}_c^{wi}$, $\mathbf{R}_c^{rp}$ The position vectors of contact points on the wheel and rail in *global frame*.

$\mathbf{t}_{1,c}^{wi}$, $\mathbf{t}_{2,c}^{wi}$ The two unit-tangent vectors to the wheel surface at the contact point in *global frame*.

ψ^t, θ^t, φ^t The Euler angles which describes the orientation of the *track frame* with respect to a *global frame*.

al, vp, gv, cl Alignment, vertical profile, gauge variation and cross level

f^{lk}, f^{rk} The value of the equivalent profiles at the lateral positions of s^{lk} and s^{rk}.

K_{hertz}, C_{damp} The Hertzian stiffness and the constant that introduces non-linear damping.

L_w The lateral distance of the *wheel frames* with respect to the wheelset frame.

R^t_x, R^t_y, R^t_z The absolute position of an arbitrary point on the ideal track centreline with respect to a *global frame* in X, Y and Z direction.

r_0 The rolling radius of the wheel when centred in the track.

s The arc-length along the track.

s^{lk}, s^{rk} The lateral positions of the contact point in the left and right KEC profiles.

y^{lir}, z^{lir}, y^{rir}, z^{rir} The track irregularities in Y and Z direction.

h^r, h^w The functions that define the railhead and wheel profiles.

s^r_1, s^r_2, s^w_1, s^w_2 The surface parameters of the railhead and wheel profiles.

$\bar{F}^{wi}_z$, $\hat{M}^{wi}_x$ The vertical force and roll torque at the wheelset due to the normal contact forces.

ν The Poisson's ratio.

A, B and β_h The parameters to compute Hertzian stiffness which depend on the curvatures of rail/wheel surfaces.

E The Young's modulus of the surface.

1. Introduction

In multibody dynamic simulation of railway vehicles, the modelling of wheel-rail contact plays a fundamental role through the literature. Contact forces and their locations within wheel and rail profiles highly influence in the dynamic behaviour of the vehicles. Hence, the development of contact models in terms of accuracy and efficiency is of great interest for the research community [1, 2, 3, 4, 5, 6]. Among these works, two well-known approaches are commonly used to simulate wheel/rail contact in multibody railway simulations. The first one is the elastic approach, in which interpenetration and separation between the wheel and rail surfaces is allowed and normal contact forces are computed, for example, using a Hertzian-based model that calculates normal contact forces using the interpenetration and interpenetration rate [7, 8, 9]. The second one is the constraint approach, where the contact between wheel and rail is computed by solving a set of nonlinear constraint equations that establish that both surfaces in contact coincide in one or more singular contact points without penetration or separation [10, 11]. In this approach, normal contact forces are described through the Lagrange multipliers, which are associated with the contact constraints at each contact point.

One main feature of the elastic and the constraint approaches is the determination of the location of the contact points. In this sense, two methodologies can be used for this contact search. On the one hand, this search can be addressed using the *online* method. In this approach, the location of the contact points is determined at each time step of the dynamic simulation by solving a set of algebraic nonlinear equations that evaluates the contact points as a function of the wheelset-track relative position. Many works can be found in the literature that use the online search method. In this sense, Marques et al. [12] present an approach to determine contact points in the conformal zone between wheel tread and flange, based on the evaluation of the contact between each wheel strip and rail avoiding inaccuracies of the minimum distance method. Magalhães et al. [13] proposed an elastic contact model for non-Hertzian conditions providing accurate results and efficient simulations. In this line, Sun et al. [14] presents a modified Kik-Piotrowski model [15] for the wheel-rail normal contact analysis, which is extended to the analysis of the influence of the wheelset yaw angle in [16]. In the work of Pombo and Ambrósio, it is proposed a three dimensional online contact detection approach to analyse the lead/lag flange contact scenarios [17], small radius track simulation [18] and the inclusion of track irregularities [19]. Moreover, in the work of O'Shea and Shabana [20, 21], the initiation of the wheel-climb phenomenon is investigated at large angles of attack. They show that the Nadal L/V derailment criteria is not conservative. In the work of Malvezzi et al. [22], two contact elastic detection methods are proposed with the known analytical expressions of the wheel and rail surfaces, one is based on the idea of minimising the distance another is minimising the difference between the surfaces. Both methods are giving efficient computational times and good agreement in terms of kinematic variables and contact forces between Matlab and Simpack Rail models in [23]. Also, Baeza et al. [24] proposed a elastic detection approach to calculate the inter-penetration areas between wheel and rail. In their work, the geometries of the wheel surface are discretised by using cones and rail head by using knife-edge lines. Moreover, in the goal of reducing the computational cost of online contact search methods, Muñoz et al. [25] presents a multibody model of railway vehicles that uses simplified contact constraints for the online wheel-tread solution combined with an elastic approach for the flange. In the same context, Escalona et al. [26] presents the simplified constraint-based wheel-rail contact method called KEC-method (Knife-edge Equivalent Contact method), in which the rails, that are considered infinitely narrow, contact an equivalent wheel profile producing the same wheelset relative-track kinematics than using real wheel-rail profiles with a great computational efficiency.

On the other hand, the search of the contact points can be done using the so-called *offline* method. In this approach, the contact solution is solved in a preprocessing stage as a function of the wheelset relative position with respect to the track, and it is stored in a lookup table, that is later used during the dynamic simulations by the interpolation in the stored data. In this sense, there are also many references that can be found in the literature about contact lookup tables. Most of them are based on the constraint approach [27, 28, 29, 30, 31, 32, 33] but also on the elastic approach [34]. The reason is that the constraint one involves a reduced relative degrees of freedom of the wheelset with respect to the track, as shown in [26]. This reduces the number of entries, and in turn the stored data, of the lookup tables. In [27], a constraint contact lookup table approach that accounts for track irregularities using two independent variables (2-DOFs) is proposed and compared with the online solution of the contact constraints. It is demonstrated that dealing carefully with geometric assumptions, simplified contact lookup tables produce accurate and efficient results. In [34], a 3-DOFs elastic contact lookup table is presented to study the advantages and disadvantages against an online procedure. The results showed that the time required for the lookup table approach is substantially lower than the online solution procedure. In [29], a combination of a constraint contact lookup table for the tread contact and an elastic online approach for the flange one is proposed and called *hybrid* method. It is extended in [30] to the combination of nodal and non-conformal contact detection, to solve significant jumps of contact points in turnouts. Moreover, in [31], a regularisation of the non-elliptical wheel-rail contact areas named Kalker book of tables for non-Hertzian contact (KBTNH) is proposed and used in [32, 33] to analyse accuracy and contact patch moments.

This paper supports and focuses on the use of the constraint approach in some applications. Clearly, the elastic approach is better suited for a more detailed contact analysis, because it allows more insight into the actual surface areas in contact. However, under some common circumstances, the use of the constraint approach is superior:

1. When the profiles geometry is not well-known, due to wear for example.
2. When the overall vehicle dynamics is of interest, instead of the intimate wheel-rail contact analysis.

In addition, as it is accepted in the community, the constraint approach is computationally more efficient. However, one of its main drawbacks is its difficult application when dealing with two-point contact scenario. This scenario is very important in curving and safety analysis of the railway vehicles. That is why this paper focuses on this scenario.

To this end, this paper compares accuracy, efficiency, applicability and limitations of two constraint-based formulations (offline and online respectively) for the dynamic simulation of the wheel-rail contact of railway vehicles in multibody dynamics. The offline methodology used in this paper is based on precalculated contact lookup tables and the online one is based on the Knife-edge Equivalent Contact method (KEC-method) presented in [26]. The use of precalculated contact lookup tables is presented first. This method is well-known, computationally efficient and widely used [27, 28, 29, 30, 31, 32, 33, 34]. It is also presented an innovative procedure to interpolate between the stored data. However, an important drawback of lookup tables appears when using wheel-rail profile combinations that show two-point contact scenarios (tread contact and flange contact) because constraint contact lookup tables are not suitable to deal with simultaneous contacts using variable number of kinematic constraints. Since most of real wheel-rail profile combinations are of this type, this scenario is essential when analysing vehicle curving or wheel climbing and derailment. Instead, the two-point contact simulation with contact lookup tables is done in this work using a hybrid method in which the flange contact is analysed using a penetration-based elastic model. The second method used in this paper is the KEC-method [26]. It is an online constraint-based method that considers the rails as infinitely narrow lines (like the edge of a knife) that contact equivalent wheels such that they show the same subspace of allowable motion that the real wheel and rail profiles. As it is a constraint-based method, the two-point contact scenario used together with a regularisation method for the tread-flange transition as presented in [35], allows possible wheel climbing.

The organisation of this paper is given as follows: Section 2 introduces the kinematics of the wheel-rail contact. Wheel-rail contact simulation with lookup tables and its interpolation procedure are presented in Section 3. The KEC-method approach is briefly explained in Section 4. Section 5 presents the generation of lookup tables for flanging wheelsets and Section 6 presents three case studies of a bogie vehicle to analyse differences and limitations of both approaches: (1) simulation results in a tangent-curved track with irregularities using profiles that do not show 2-point contacts, (2) simulation results in a tangent-curved track with irregularities using profiles that show 2-point contacts and (3) simulation results of a wheel climbing scenario in a small radius curved track without irregularities. Finally, Section 7 provides a summary and conclusion.

2. Kinematics of the wheel-rail contact

2.1. Track kinematics

Track geometry is the superposition of the ideal geometry and the irregularities. The components of the absolute position vector of an arbitrary point on the ideal track centreline with respect to a global frame is a function of the arc-length s, as follows:

$$\mathbf{R}^t(s) = \begin{bmatrix} R_x^t(s) \\ R_y^t(s) \\ R_z^t(s) \end{bmatrix}, \tag{1}$$

where $\mathbf{R}^t(s)$ contains the components of vector $\overrightarrow{R}^t$ shown in Fig. 1. The geometry of the track centreline 3D-curve is defined by the *horizontal profile* and the *vertical profile*. The so-called track preprocessors implement these functions of s given the ideal track geometry using a set of segment-dependent parameters (length, curvature, slope, etc.)

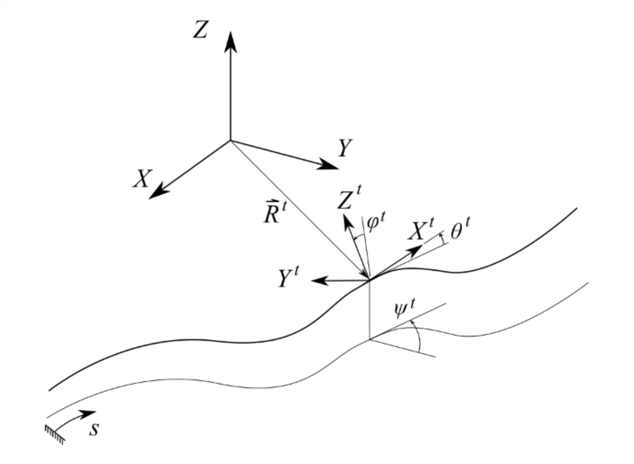

Fig. 1: Ideal track centreline.

Figure 1 shows the track frame $\langle O^t; X^t, Y^t, Z^t \rangle$ associated with the track centreline at each value of s. The orientation of the track frame with respect to a global frame can be measured with the Euler angles ψ^t (*azimut* or *heading* angle), θ^t (vertical slope, positive when downwards in the forward direction) and φ^t (*cant* or *superelevation* angle). These three angles are also functions of s that are implemented in the track pre-processor. The rotation matrix from the track frame to the global frame is given by:

$$\mathbf{A}^t(s) = \begin{bmatrix} \mathrm{c}\theta^t \mathrm{c}\psi^t & \mathrm{s}\varphi^t \mathrm{s}\theta^t \mathrm{c}\psi^t - \mathrm{c}\varphi^t \mathrm{s}\psi^t & \mathrm{s}\varphi^t \mathrm{s}\psi^t + \mathrm{c}\varphi^t \mathrm{s}\theta^t \mathrm{c}\psi^t \\ \mathrm{c}\theta^t \mathrm{s}\psi^t & \mathrm{c}\varphi^t \mathrm{c}\psi^t + \mathrm{s}\varphi^t \mathrm{s}\theta^t \mathrm{s}\psi^t & \mathrm{c}\varphi^t \mathrm{s}\theta^t \mathrm{s}\psi^t - \mathrm{s}\varphi^t \mathrm{c}\psi^t \\ -\mathrm{s}\theta^t & \mathrm{s}\varphi^t \mathrm{c}\theta^t & \mathrm{c}\varphi^t \mathrm{c}\theta^t \end{bmatrix}. \tag{2}$$

where the terms ‘c’ and ‘s’ in Eq. 2 refer to the cosine and sine functions respectively.

Figure 2 on the left shows the relative position of the irregular right rail centreline with respect to the track frame. Figure 2 on the right shows the displacement of the railheads due to irregularity in a cross-section of the track ($Y^t - Z^t$ plane). As observed in the figure, a frame is defined at each railhead (lrp, *left rail profile* frame, and rrp, *right rail profile* frame). Left and right rail profile frames are separated a distance $2L_r$ in the ideal track. The irregularity vectors $\overrightarrow{r}^{lir}$ (lir, *left rail irregularity*) and $\overrightarrow{r}^{rir}$ (rir, *right rail irregularity*) describe the displacement of the rail centrelines. The components of these vectors in the track frame are functions of s, given by:

$$\bar{\mathbf{r}}^{lir}(s) = \begin{bmatrix} 0 \\ y^{lir} \\ z^{lir} \end{bmatrix}, \qquad \bar{\mathbf{r}}^{rir}(s) = \begin{bmatrix} 0 \\ y^{rir} \\ z^{rir} \end{bmatrix} \tag{3}$$

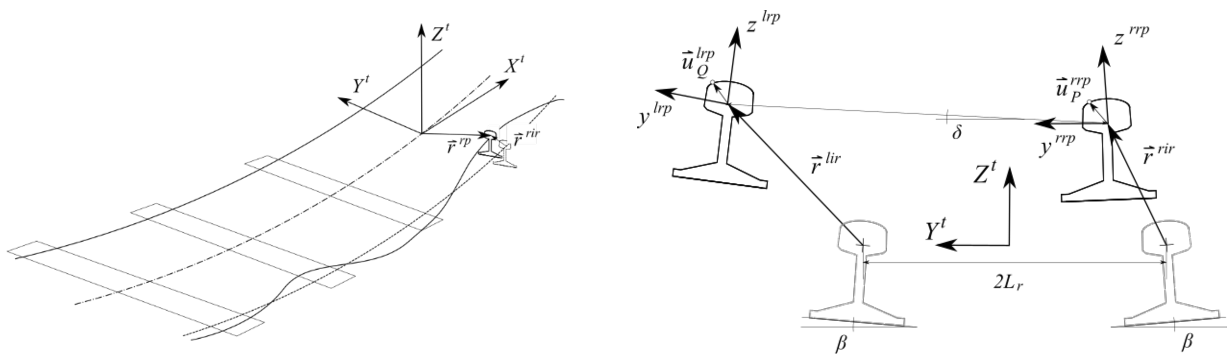

Fig. 2: Track irregularity.

In the railway industry, the following four combinations of the railhead centrelines irregularities are measured:

- Alignment(al) : $al = (y^{lir} + y^{rir})/2$
- Verticle profile(vp) : $vp = (z^{lir} + z^{rir})/2$
- Gauge variation(gv) : $gv = y^{lir} - y^{rir}$
- Cross level(cl) : $cl = z^{lir} - z^{rir}$

The orientation of the railhead frames with respect to the track frame is given by the following rotation matrices:

$$\mathbf{A}^{t,lrp}(s) = \begin{bmatrix} 1 & 0 & 0 \\ 0 & \cos(\beta+\delta) & -\sin(\beta+\delta) \\ 0 & \sin(\beta+\delta) & \cos(\beta+\delta) \end{bmatrix}, \quad \mathbf{A}^{t,rrp}(s) = \begin{bmatrix} 1 & 0 & 0 \\ 0 & \cos(-\beta+\delta) & -\sin(-\beta+\delta) \\ 0 & \sin(-\beta+\delta) & \cos(-\beta+\delta) \end{bmatrix}, \tag{4}$$

where β is the orientation angle of the rail profiles and $\delta = (z^{lir} - z^{rir})/2L_r$ is the linearized rotation angle due to the irregularity. Both angles can be observed in Fig. 2 on the right.

The absolute position vectors of two points, P and Q, defined in the right and left railheads, respectively, are given by:

$$\begin{aligned}\overrightarrow{R}_P^{rrp} &= \overrightarrow{R}^t + \overrightarrow{r}^{rrp} + \overrightarrow{r}^{rir} + \overrightarrow{u}_P^{rrp}.\\ \overrightarrow{R}_Q^{lrp} &= \overrightarrow{R}^t + \overrightarrow{r}^{lrp} + \overrightarrow{r}^{lir} + \overrightarrow{u}_Q^{lrp}.\end{aligned} \tag{5}$$

The components of these vectors in the global frame are given by:

$$\begin{aligned}\mathbf{R}_P^{rrp} &= \mathbf{R}^t + \mathbf{A}^t(\bar{\mathbf{r}}^{rrp} + \bar{\mathbf{r}}^{rir} + \mathbf{A}^{t,rrp}\hat{\mathbf{u}}_P^{rrp}),\\ \mathbf{R}_Q^{lrp} &= \mathbf{R}^t + \mathbf{A}^t(\bar{\mathbf{r}}^{lrp} + \bar{\mathbf{r}}^{lir} + \mathbf{A}^{t,lrp}\hat{\mathbf{u}}_Q^{lrp}),\end{aligned} \tag{6}$$

where $\hat{\mathbf{u}}_P^{rrp}$ and $\hat{\mathbf{u}}_Q^{lrp}$ contain the components of the position vector of points P and Q in the rail profiles as shown in Fig. 2 on the right. These vectors are parametrized following the railhead profile geometry:

$$\hat{\mathbf{u}}_P^{rrp} = \begin{bmatrix} 0 \\ s_2^{rr} \\ h^{rr}(s_2^{rr}) \end{bmatrix}, \qquad \hat{\mathbf{u}}_Q^{lrp} = \begin{bmatrix} 0 \\ s_2^{lr} \\ h^{lr}(s_2^{lr}) \end{bmatrix}, \tag{7}$$

where lr and rr stand for *left rail* and *right rail*, s_2^{lr} and s_2^{rr} are the transverse coordinates of the points in the railheads and h^{lr} and h^{rr} are the functions that define the railhead profile, as shown in Fig. 3.

The calculation of the track geometry requires interpolation at two levels: (1) the description of the centreline shown in Eq. (1) as a function of the longitudinal arc-length s and (2) the description of the rail-head cross sections h^{lr} and h^{rr} shown in Eq. (7) as a function of the transverse parameters s_2^{lr} and s_2^{rr}. Both are implemented in this investigation using cubic splines. For the description of the track centreline, the analytic functions used in the industry to describe the track horizontal and vertical profiles (straight lines, circles, clothoids and cubic polynomials) are used to tabulate the absolute position a set of equally-spaced nodal points. For the description of the rail-head profiles, the straight lines and circles used to define the new (not worn) rail-head profiles are used to tabulate the functions h^{lr} and h^{rr} at a set of nodal points. Alternatively, experimentally measured rail-head profiles can be used if worn rail-head profiles are simulated. The benefits of the cubic interpolation compared with the evaluation of analytic functions is the smoothness of the higher-order space-derivatives of the geometry at the transition points.

2.2. Vehicle kinematics

For the modelling of a railway vehicle, a set of relative body-track frame coordinates, as shown in Fig. 4, is selected in this work. In this formulation [26], each modelled body belonging to the railway vehicle is accompanied by a track-frame along the track centreline. These frames are called *body-track frames* $\langle O^{bti}; X^{bti}, Y^{bti}, Z^{bti}\rangle$ for each body i. The body-track frame is defined such that the relative position vector $\bar{\mathbf{r}}^i = \begin{bmatrix} 0 & \bar{r}_y^i & \bar{r}_z^i \end{bmatrix}^T$ of the body frame with respect to the body-track

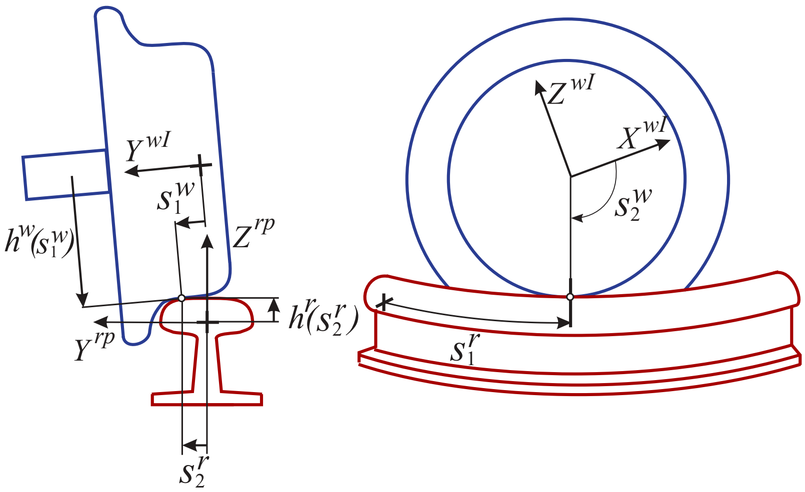

Fig. 3: Wheel profile and rail profile geometry.

frame has zero x-component along the track centreline. Therefore, for each body i, the following set of coordinates is defined:

$$\mathbf{q}^i = \begin{bmatrix} s^i & \bar{r}_y^i & \bar{r}_z^i & (\bar{\mathbf{\Phi}}^i)^T \end{bmatrix}^T = \begin{bmatrix} s^i & \bar{r}_y^i & \bar{r}_z^i & \bar{\varphi}^i & \bar{\theta}^i & \bar{\psi}^i \end{bmatrix}^T, \tag{8}$$

where the vector $\mathbf{q}^i$ describes the absolute position of the body track frame (arc-length coordinate s^i), the relative body frame to body-track frame position (position vector $\bar{\mathbf{r}}^i$) and relative body frame to body-track frame orientation (Euler angles $\bar{\mathbf{\Phi}}^i$). Therefore, the set of coordinates for all vehicle bodies is:

$$\mathbf{q} = \begin{bmatrix} \mathbf{q}^2 \\ \vdots \\ \mathbf{q}^{nb} \end{bmatrix}, \tag{9}$$

where nb is the number of modelled bodies in the railway vehicle. Superscripts start at 2 because body 1 is assumed to be the ground body, this is, the track.

Using these coordinates, the absolute position vector of point P that belongs to body i is given by:

$$\overrightarrow{R}_P^i = \overrightarrow{R}^{bti} + \overrightarrow{r}^i + \overrightarrow{u}_P^i. \tag{10}$$

where $\overrightarrow{R}_P^i$ (not shown in Fig. 1) is the absolute position vector of P, $\overrightarrow{R}^{bti}$ is the absolute position vector of the body-track frame, $\overrightarrow{r}^i$ is the relative position vector of the origin of the body i frame with respect to its body-track frame and $\overrightarrow{u}_P^i$ is the local position vector of point P in body i. Equation (10) can be projected in the global frame as follows:

$$\mathbf{R}_P^i = \mathbf{R}^{bti} + \mathbf{A}^{bti}(\bar{\mathbf{r}}^i + \mathbf{A}^{bti,i}\hat{\mathbf{u}}_P^i). \tag{11}$$

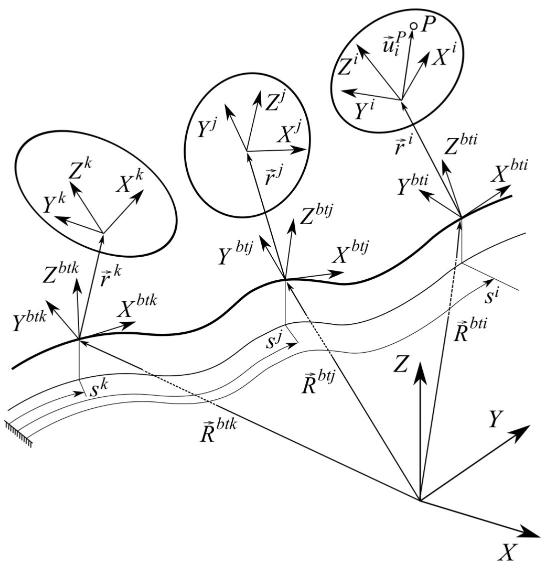

Fig. 4: Kinematics of the bodies of a railway vehicle with relative body-track frame coordinates.

In this formula, the terms have the following meaning and functional dependency:

$\mathbf{R}^{bti} = \mathbf{R}^{bti}(s^i)$	Components of position vector of the body-track frame in the global frame.
$\mathbf{A}^{bti} = \mathbf{A}^{bti}(s^i)$	Transformation matrix of the body-track frame to the global frame.
$\bar{\mathbf{r}}^i = \bar{\mathbf{r}}^i(\mathbf{q})$	Components of position vector of the body with respect to the body-track frame in the body-track frame.
$\mathbf{A}^{bti,i} = \mathbf{A}^{bti,i}(\mathbf{q})$	Transformation matrix of the base body frame with respect to the body-track frame.
$\hat{\mathbf{u}}^i_P$	Components of the position vector of point P with respect to body i in the body frame. These components are constant.

2.3. Wheelset kinematics

The track-relative coordinates of a rigid wheelset i (superscript wi) are:

$$\mathbf{q}^{wi} = \begin{bmatrix} s^{wi} & \bar{r}_y^{wi} & \bar{r}_z^{wi} & \bar{\varphi}^{wi} & \bar{\theta}^{wi} & \bar{\psi}^{wi} \end{bmatrix}^T. \tag{12}$$

For each rigid wheelset, an additional frame that rotates with the wheelset without following the rolling angle $\bar{\theta}^{wi}$ is defined: the *wheelset intermediate frame, wIi*. Figure 5 shows the wheelset i body frame wi and the intermediate one wIi. The orientation of the wheelset body frame with respect to the wheelset track frame wti is given by the following matrix:

$$\mathbf{A}^{wti,wi} = \mathbf{A}^{wti,wIi}(\bar{\psi}^{wi}, \bar{\varphi}^{wi})\mathbf{A}^{wIi,wi}(\bar{\theta}^{wi}), \tag{13}$$

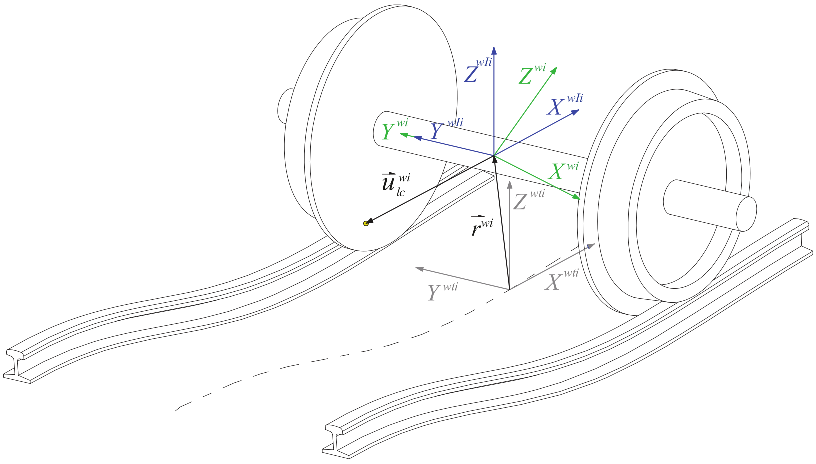

Fig. 5: Frames for rigid wheelset kinematics.

where the brackets mean the functional dependency of the rotation matrices.

The use of the wheelset intermediate frame allows a clearer description of the position of the wheel-rail contact points. This position varies very little in the wIi frame, but it greatly varies in the wi frame (this variation is approximately periodic, being the time taken by the wheel to complete a revolution the time-period). The position vector of an arbitrary point P on the surface of the left or right wheel profile can be obtained as:

$$\mathbf{R}_P^{wi} = \mathbf{R}^{wti} + \mathbf{A}^{wti}(\bar{\mathbf{r}}^{wi} + \mathbf{A}^{wti,wIi}\hat{\mathbf{u}}_P^{wIi}), \tag{14}$$

where $\hat{\mathbf{u}}_P^{wIi}$ may take the following forms for the left ($P = L$) or right wheels ($P = R$):

$$\hat{\mathbf{u}}_R^{wIi} = \begin{bmatrix} h^{rw}(s_1^{rw})\cos s_2^{rw} \\ -L_w + s_1^{rw} \\ -h^{rw}(s_1^{rw})\sin s_2^{rw} \end{bmatrix}, \qquad \hat{\mathbf{u}}_L^{wIi} = \begin{bmatrix} h^{lw}(s_1^{lw})\cos s_2^{lw} \\ L_w + s_1^{lw} \\ -h^{lw}(s_1^{lw})\sin s_2^{lw} \end{bmatrix}, \tag{15}$$

where lw and rw stand for *left wheel* and *right wheel*, s_1^{lw}, s_2^{lw}, s_1^{rw} and s_2^{rw} are the parameters needed to the define the points in the wheel surface, h^{lw} and h^{rw} are the functions that defines the left and right wheel profile, as shown in Fig. 3 and L_w is the lateral distance of the wheel frames with respect to the wheelset frame.

2.4. Wheel-rail contact constraints

The wheel-rail non-conformal contact constraints (see Fig. 6) establish that the absolute position of the contact point on the rail is the same as the absolute position of the contact point on the wheel. In addition, the tangent plane to the rail at the contact point is parallel to the tangent plane to the wheel at the contact point. These are five constraint equations that can written as:

$$
\begin{aligned}
&\mathbf{R}_c^{wi}(\mathbf{q}^{wi}, \mathbf{s}^w) - \mathbf{R}_c^{rp}(\mathbf{s}^r) = \mathbf{0}, \\
&\left[\mathbf{t}_{1,c}^{wi}(\mathbf{q}^{wi}, \mathbf{s}^w)\right]^T \mathbf{n}_c^{rp}(\mathbf{s}^r) = 0, \\
&\left[\mathbf{t}_{2,c}^{wi}(\mathbf{q}^{wi}, \mathbf{s}^w)\right]^T \mathbf{n}_c^{rp}(\mathbf{s}^r) = 0,
\end{aligned}
\tag{16}
$$

where c can be lc (left contact) or rc (right contact), w can be lw (left wheel) or rw (right wheel), rp can be lrp (left rail profile) or rrp (right rail profile), $\mathbf{s}^w = \begin{bmatrix} s_1^w & s_2^w \end{bmatrix}^T$, $\mathbf{s}^r = \begin{bmatrix} s_1^r & s_2^r \end{bmatrix}^T$ include all surface parameters needed to locate the contact points, $\mathbf{t}_{1,c}^{wi}$ and $\mathbf{t}_{2,c}^{wi}$ are the two unit-tangent vectors to the wheel surface at the contact point, $\mathbf{n}_c^{rp}$ is the normal vector to the rail surface at the contact point.

The tangent vectors $\mathbf{t}_{1,c}^{wi}$ and $\mathbf{t}_{2,c}^{wi}$ from Eq. (16), which are defined with respect to the surface parameters $\mathbf{s}^w$, span the tangent plane at the contact point. $\mathbf{t}_{1,c}^{wi}$ is perpendicular to the cross-section and $\mathbf{t}_{2,c}^{wi}$ lies in it. The normal vector $\mathbf{n}_c^{rp}$ is defined as the cross-product of the two tangent vectors.

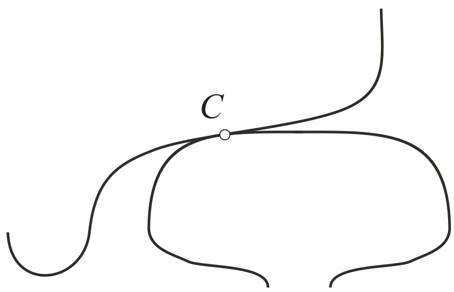

Fig. 6: Wheel and rail in contact.

The approximate contact constraints represent a simplified version to Eq. (16). The approximate contact constraints neglect the influence of the wheelset yaw angle in the contact geometry. In other words, the 3D surface-to-surface contact constraints are reduced to 2D curve-to-curve contact constraints. The main implication of this approach is that the so-called lead-lag contact effect, that occurs due to the longitudinal displacement of the flange contact point with respect to the thread contact point, is neglected. The lead-lag contact effect has, in practice, influence in the vehicle motion when negotiating very narrow curves. This curve negotiation usually happens at very low velocities following a quasi-static motion. As shown in [27], the planar contact approach is commonly sufficiently accurate. The approximate contact constraints can be written as a set of three constraint equations per wheel-rail pair as follows:

$$
\begin{aligned}
&\bar{\mathbf{r}}_c^{wi}(\mathbf{q}^{wi}, s_1^w) - \bar{\mathbf{r}}_c^{rp}(s_2^r) = \mathbf{0}, \\
&\left[\bar{\mathbf{t}}_{1,c}^{wi}(\mathbf{q}^{wi}, s_1^w)\right]^T \bar{\mathbf{n}}_c^{rp}(s_2^r) = 0,
\end{aligned}
\tag{17}
$$

In these equations, vectors are projected to the track frame. Due to the assumed 2D contact approach, the X-component of the vector equation on top is automatically fulfilled, because both vectors $\bar{\mathbf{r}}_c^{wi}$ and $\bar{\mathbf{r}}_c^{rp}$ are contained in the Y-Z plane of the track frame. Therefore, only the Y-Z components are used. Accordingly, the perpendicularity of $\bar{\mathbf{n}}_c^{rp}$ and $\bar{\mathbf{t}}_{2,c}^{wi}$ is guaranteed as well. Hence, the total set of equations in Eq. (17) is reduced to 3. The 2D contact approach also implies that $s_2^w = \pi/2$ and $s_1^r = s^w$. Only one surface parameter per profile needs to be indentified. In practice, the set of surface parameters is reduced from 4 to 2. For that reason, the simplified nomenclature $s^w = s_1^w$ and $s^r = s_2^r$ will be used. More details about the use of these contact constraints for non-conformal contacts can be found in [27].

3. Wheel-rail contact simulation with lookup tables

This section explains the use of contact lookup tables for the simulation of railway vehicles using relative body-track frame coordinates.

3.1. Calculation of lookup tables

Lookup tables are calculated in a preprocessing stage. To create a contact lookup table, a set of discrete numerical values is assigned to the lateral displacement of the wheelset y^{wi} in a range that will be discussed in Section 5. The position along the track s^{wi} and pitch angle θ^{wi} are assumed to be zero because these coordinates have no influence on the contact geometry. The yaw angle ψ^{wi} is also assumed to be zero because its influence in the contact geometry is assumed to be negligible, as explained in Section 2.4. For each of these positions, 6 simplified contact constraints Eq. (17) (3 for left contact and 3 for right contact) are solved to find the values of 6 coordinates: the wheelset position and orientation coordinates z^{wi} and roll angle φ^{wi} and the surface parameters s^{lw}, s^{rw}, s^{lr} and s^{rr} needed to locate the contact points on the left and right wheel and rail surfaces. The contact lookup table can be interpreted as a set of tabulated functions of the form:

$$
\begin{aligned}
&z^{wi} = z_{clt}(y^{wi}), \quad \varphi^{wi} = \varphi_{clt}(y^{wi}), \\
&s^{lw} = s^{lw}_{clt}(y^{wi}), \quad s^{lr} = s^{lr}_{clt}(y^{wi}) \quad s^{rw} = s^{rw}_{clt}(y^{wi}), \quad s^{rr} = s^{rr}_{clt}(y^{wi}),
\end{aligned}
\tag{18}
$$

where the subscript *clt* stands for 'contact lookup table'. The contact lookup table can be used in dynamic simulations to find the values of these six coordinates from the value of the lateral displacement. In order to deal with a track with irregularities, the contact lookup table has to be extended from 1 entry to 2 entries. The process of creation of the contact lookup table has to be repeated for a set of values of the gauge variation (gv) in a range that covers the extreme values of the gauge that appear in practical applications. This is, the contact lookup table is recalculated a number of times after approaching and separating the rails from the nominal distance $2L_r$ shown in Fig. 2. That way, the functions given above become functions of two variables, as follows:

$$
\begin{aligned}
&z^{wi} = z_{clt}(y^{wi}, gv), \quad \varphi^{wi} = \varphi_{clt}(y^{wi}, gv) \\
&s^{lw} = s^{lw}_{clt}(y^{wi}, gv), \quad s^{lr} = s^{lr}_{clt}(y^{wi}, gv) \quad s^{rw} = s^{rw}_{clt}(y^{wi}, gv), \quad s^{rr} = s^{rr}_{clt}(y^{wi}, gv)
\end{aligned}
\tag{19}
$$

The use of the lookup tables with irregular track is slightly different. In a dynamic simulation, given the longitudinal position of the wheelset s^{wi} , the values of the irregularities al, vp, gv and cl can be obtained. The lateral displacement that has to be used to enter the lookup table is not y^{wi} that gives the lateral displacement with respect to the ideal track centreline, but $\bar{y}^{wi} = y^{wi} - al$, that gives the lateral displacement with respect to the irregular track centreline. In turn, the outputs of the lookup table $\bar{z}^{wi}$ and $\bar{\varphi}^{wi}$ have to be interpreted differently, being $\bar{z}^{wi} = z^{wi} + vp$ and $\bar{\varphi}^{wi} = \varphi^{wi} + cl/2L_r$. The kinematic constraints associated with wheelset wi finally yield:

$$\mathbf{C}^{clt,wi} = \begin{bmatrix} z^{wi} - vp - z_{clt}(\bar{y}^{wi} + al, gv) \\ \varphi^{wi} - cl/2L_r - \varphi_{clt}(\bar{y}^{wi} + al, gv) \end{bmatrix} = \mathbf{0}. \tag{20}$$

More details in railway multibody simulation using contact lookup tables can be found in [27].

3.2. Interpolation in the lookup tables

As explained in the previous sections, for the generation of KEC-profiles and also during the simulation with the KEC-method, the lookup tables have to be used to find the location of the contact points in the real profiles and other geometric properties. This sub-section describes the interpolation in the lookup tables in these cases. However, when using the lookup table contact method with elastic contact in the flange, the lookup tables that are used do not account for contact constraints in the flange (penetration is assumed to occur instead). Therefore, the content of this section is not applicable in that case.

In this context, the use of contact lookup tables that consider flange contact constraints (this is, wheel climb is admissible without flange penetration) and also include track irregularities, requires a special treatment in the interpolation procedure. In what follows and with the help of Fig. 7 (superscript wi is omitted in the figure for simplicity), it is shown the error obtained when the interpolation is applied in the vicinity of the two-point of flange contact scenario.

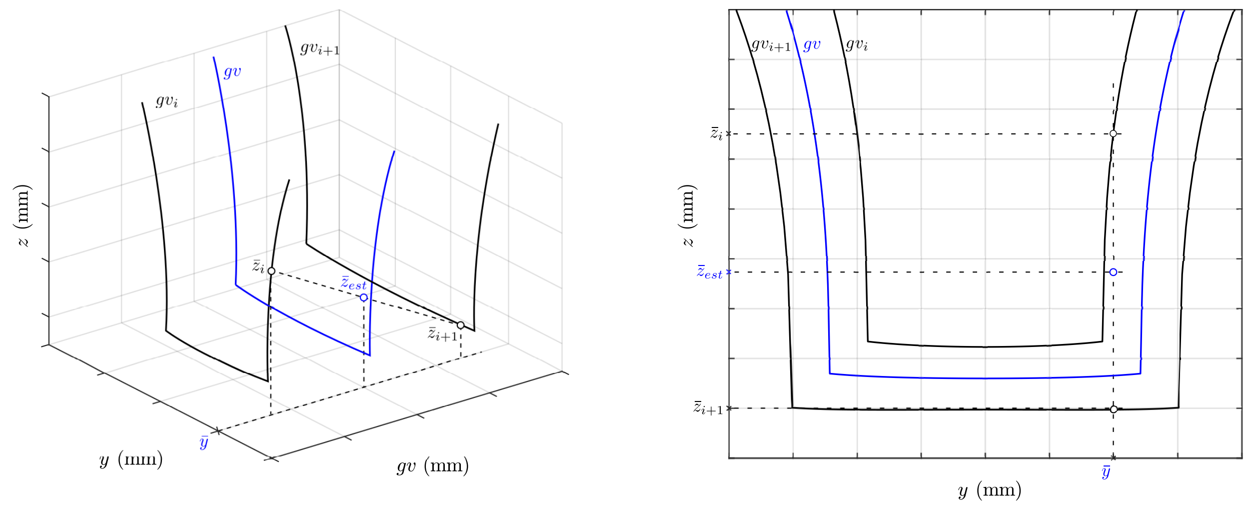

Fig. 7: Interpolation error at contact lookup tables with track irregularities.

Figure 7 shows in solid dark lines the wheelset vertical coordinate $\bar{z}^{wi}$ stored in the lookup table for two different values of gauge irregularity (gv_i and gv_{i+1}) and in solid blue line the same for an arbitrary track gauge irregularity gv between gv_i and gv_{i+1} that is not stored in the table. Let us assume that in a specific instant of a simulation with track gauge gv (solutions given in blue line that are not stored in the table), the wheelset lateral displacement $\bar{y}^{wi}$ is in the vicinity of the two-point wheel-rail contact scenario such that, in order to interpolate in table gv_{i+1} with $\bar{y}^{wi}$ the wheelset is at a single point tread contact $\bar{z}^{wi}_{i+1}$, while in table gv_i the wheelset is at a wheel climb scenario $\bar{z}^{wi}$. Obviously, the interpolation between $\bar{z}^{wi}_i$ and $\bar{z}^{wi}_{i+1}$ provides an estimated wheelset vertical displacement $\bar{z}^{wi}_{est}$ that is far from the correct value given by the blue line as shown in Fig. 7.

In order to avoid these interpolation errors, the wheelset lateral displacement $\bar{y}^{wi}$ cannot be used directly as an input to interpolate in the tables. It has to be updated to the values $\bar{y}^{wi}_i$ and $\bar{y}^{wi}_{i+1}$ that correspond to gauge variations gv_i and gv_{i+1} that are stored in the table. This procedure, which is shown in Fig. 8, is defined as follows:

- Given $\bar{y}^{wi}$ and gv , find the point of convergence O and its theoretical irregularity gv_O as:

$$gv_O = gv_{i+1} - \frac{\bar{y}^f_{i+1} \cdot (gv_{i+1} - gv_i)}{\bar{y}^f_{i+1} - \bar{y}^f_i} \tag{21}$$

  where superscript f refers to the flange starting point. Note that gv_O is a conceptual gauge irregularity in which both wheels experience flange contact and the wheelset has no possible lateral displacement.

- Interpolate in the direction $O - \bar{y}^{wi}$ to obtain the corresponding two lateral displacements $\bar{y}^{wi}_i$ and $\bar{y}^{wi}_{i+1}$.

- Enter the lookup tables gv_i and gv_{i+1} with $\bar{y}^{wi}_i$ and $\bar{y}^{wi}_{i+1}$ to obtain the contact solutions at the stored tables (i.e. $\bar{z}^{wi}_i$ and $\bar{z}^{wi}_{i+1}$ for the vertical displacement, $\bar{\varphi}^{wi}_i$ and $\bar{\varphi}^{wi}_{i+1}$ for the roll angle).

- Interpolate between the stored solutions to obtain the accurate coordinate (i.e. $\bar{z}^{wi}_{est}$ and $\bar{\varphi}^{wi}_{est}$).

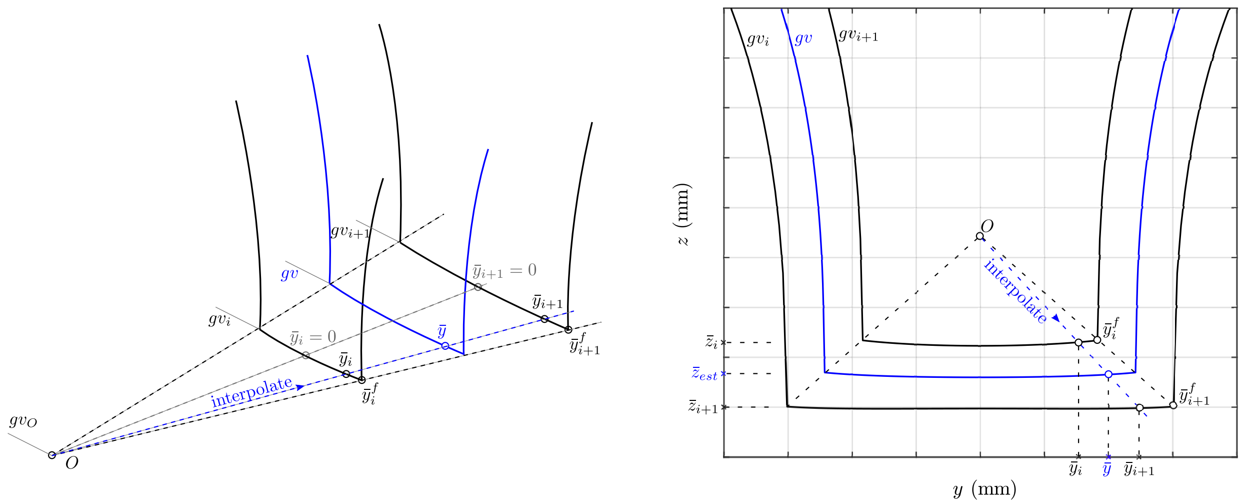

Fig. 8: Interpolation method at contact lookup tables with track irregularities.

As it is shown by Fig. 7 and Fig. 8, the described linear interpolation procedure avoids errors that can be considerably high in the vicinity of the flange contact scenario.

3.3. Calculation of contact forces when using lookup tables

Contact forces are divided into normal contact forces and tangential contact forces. When using lookup tables, normal contact forces in the tread are computed as reaction forces associated with the contact constraints, while normal contact forces in the flange are computed as elastic forces as a function of the wheel-rail penetration. For both, tread and flange contact, tangential contact forces are computed as applied forces using any established creep contact theory (as Kalker non-linear theory [36] or Polach theory [37]). The resulting equations of motion of the railway vehicle yield:

$$\begin{bmatrix} \mathbf{M} & \left(\mathbf{C}_{\mathbf{q}}^{clt}\right)^{T} \\ \mathbf{C}_{\mathbf{q}}^{clt} & \mathbf{0} \end{bmatrix} \begin{bmatrix} \ddot{\mathbf{q}} \\ \boldsymbol{\lambda} \end{bmatrix} = \begin{bmatrix} \mathbf{Q} + \mathbf{Q}_{fla}^{nor} + \mathbf{Q}^{tang} \\ -\dot{\mathbf{C}}_{\mathbf{q}}^{clu} \dot{\mathbf{q}} \end{bmatrix} \tag{22}$$

where $\mathbf{M}$ is the vehicle mass matrix, $\mathbf{C}_{\mathbf{q}}^{clt}$ is the Jacobian matrix of all wheel-rail contact constraints modelled with lookup tables, $\boldsymbol{\lambda}$ is the array of Lagrange multipliers, $\mathbf{Q}_{fla}^{nor}$ is the vector of generalised wheel-rail normal flange forces, $\mathbf{Q}^{tang}$ is the vector of generalised tangential tread and flange forces, and $\mathbf{Q}$ include all other generalised applied forces and generalised quadratic-velocity inertia forces. For clarity, in this equation it has been assumed that the only constraints in the vehicle system are those due to the wheel rail contact. However, everything is valid under the existence of other constraints.

The generalised normal forces at the wheel tread are computed using the Lagrange multipliers technique. Therefore, these forces are treated as reaction forces whose value can be computed as:

$$\mathbf{Q}_{tread}^{nor} = -\left(\mathbf{C}_{\mathbf{q}}^{clt}\right)^{T} \boldsymbol{\lambda}. \tag{23}$$

The Jacobian matrix $\mathbf{C}_{\mathbf{q}}^{clt}$ is an assembly of the Jacobian matrices $\mathbf{C}_{\mathbf{q}}^{clt,wi}$ associated with each wheelset, that is given by:

$$\mathbf{C}_{\mathbf{q}}^{clt,wi} = \begin{bmatrix} -\frac{\mathrm{d}vp}{\mathrm{d}s^{wi}} - \frac{\partial z_{clt}}{\partial y}\frac{\mathrm{d}al}{\mathrm{d}s^{wi}} - \frac{\partial z_{clt}}{\partial gv}\frac{\mathrm{d}gv}{\mathrm{d}s^{wi}} & -\frac{\partial z_{clt}}{\partial y} & 1 & 0 & 0 & 0 \\ -\frac{1}{2L_r}\frac{\mathrm{d}cl}{\mathrm{d}s^{wi}} - \frac{\partial \varphi_{clt}}{\partial y}\frac{\mathrm{d}al}{\mathrm{d}s^{wi}} - \frac{\partial \varphi_{clt}}{\partial gv}\frac{\mathrm{d}gv}{\mathrm{d}s^{wi}} & -\frac{\partial \varphi_{clt}}{\partial y} & 0 & 1 & 0 & 0 \end{bmatrix} \tag{24}$$

In this matrix the fact that the irregularities al, vp, gv and cl are a functions of the wheelset position along the track s^{wi}, has been accounted for. However, because these functions use to be such that the derivatives with respect to s^{wi} are very small, the Jacobian matrix can be simplified to:

$$\mathbf{C}_{\mathbf{q}}^{clt,wi} = \begin{bmatrix} 0 & -\frac{\partial z_{clt}}{\partial y} & 1 & 0 & 0 & 0 \\ \\ 0 & -\frac{\partial \varphi_{clt}}{\partial y} & 0 & 1 & 0 & 0 \end{bmatrix} \tag{25}$$

The use of Eq. (24) would be needed if the wave-length of the track irregularities were short compared with the distance advanced by the wheel in one time-step. In practise, the measured irregularities have wave-lengths above 1 m, that is much longer than that distance.

The generalised normal forces at the wheel flange are treated as applied forces. The contact point detection at flange can be obtained offline, while building the contact lookup table. Thus, the maximum relative-indentation condition [27] is used for potential contact point search at flange, which is:

$$\begin{aligned} &\left[\bar{\mathbf{t}}_{1,c}^{wi}(\mathbf{q}^{wi}, s_{fla,1}^{w})\right]^T (\bar{\mathbf{r}}_c^{wi}(\mathbf{q}^{wi}, s_{fla,1}^{w}) - \bar{\mathbf{r}}_c^{rp}(s_{fla,2}^{r})) = 0, \\ &\left[\bar{\mathbf{t}}_{1,c}^{wi}(\mathbf{q}^{wi}, s_{fla,1}^{w})\right]^T \bar{\mathbf{n}}_c^{rp}(s_{fla,2}^{r}) = 0, \end{aligned} \tag{26}$$

Note that the vectors are projected to the Y-Z plane of the track frame. Equation (26) is a set of two nonlinear equations of two unknown variables; the flange surface parameters at the wheel and the rail, $s_{fla,1}^{w}$ and $s_{fla,2}^{r}$, which can be solved using the Newton-Raphson method. The indentation δ^{wi} at flange is computed as:

$$\delta^{wi} = \left[\bar{\mathbf{r}}_c^{wi} - \bar{\mathbf{r}}_c^{rp}\right]^T \bar{\mathbf{n}}_c^{wi} \tag{27}$$

In this research, the flange normal contact force at wheelset i (wi) is computed based on a Hunt-Crossley force model [27, 8, 38], including the elastic and dissipative components:

$$\begin{aligned} \mathbf{Q}_{fla}^{nor,wi} &= \left(\frac{\partial \bar{\mathbf{r}}_{fla}^{wi}}{\partial \mathbf{q}^{wi}}\right)^T \mathbf{F}_{fla}^{nor,wi}, \\ \mathbf{F}_{fla}^{nor,wi} &= \begin{cases} K_{hertz}(\delta^{wi})^{3/2} + C_{damp}\dot{\delta}^{wi}\delta^{wi} & \text{if} \quad \delta^{wi} > 0 \\ \mathbf{0} & \text{if} \quad \delta^{wi} \leq 0 \end{cases}, \end{aligned} \tag{28}$$

where $\bar{\mathbf{r}}_{fla}^{wi}$ is the position vector of the contact point in the flange, $\mathbf{F}_{fla}^{nor,wi}$ is the elastic normal force in the flange, δ^{wi} is the wheel-rail penetration at the flange contact, K_{hertz} is the Hertzian stiffness and C_{damp} is a constant that introduces non-linear damping. Note that the terms $\bar{\mathbf{r}}_{fla}^{wi}$, δ^{wi} and K_{hertz} are interpolated from the lookup table.

The Hertzian stiffness K_{hertz} can be obtained based on the curvatures and material properties of the wheel and rail surfaces [39]:

$$K_{hertz} = \frac{4\beta_h}{3(K_i + K_j)\sqrt{A+B}}, \quad K_k = \frac{1-\nu_k^2}{\pi E_k} \tag{29}$$

where ν_k is the Poisson's ratio and E_k is is the the Young's modulus of surface k, A, B and β_h are computed based on the curvatures of both surfaces (see [39, 40]). However, this formula that comes from Hertz contact theory, assumes that the bodies in contact behave like infinite semi-spaces. Thus, the contact stiffness can be modified (decreased) to account for the structural deformation of the bodies. This structural deformation can be important in the wheel flange.

For the calculation of the contact-tangential creep forces that result in $\mathbf{Q}^{tang}$, the following data are needed for each wheel-rail contact pair (either tread or flange contact):

1. The normal contact force.
2. The relative velocity of the contact points
3. Kalker's constants and coefficient of friction

Here, two problems arise just for the tread contacts:

1. The generalised normal forces $\mathbf{Q}^{nor}_{tread}$ (reaction forces) are known only after solving Eq. (20) and
2. The calculation of the normal force at wheelset wi, $\mathbf{F}^{nor,wi}_{tread}$, from the generalised normal force $\mathbf{Q}^{nor}_{tread}$ is not straight forward.

The solution to the first problem, that being strict would require an iterative solution of the equations of motion Eq. (22), is practically solved by assuming that the normal forces this time-step equal the normal forces obtained last time-step. This simple assumption works efficiently in practice because general time-steps used in railway multibody simulations are usually small (a maximum of around 1 ms). Also, to the best Authors' knowledge, there are no simulation codes that implement such iterative procedure to find the tangential forces.

For the second problem, the following approach is derived: the vertical force $\bar{F}_z^{wi}$ (vertical component in the track frame) and roll torque $\hat{M}_x^{wi}$ (longitudinal component in the wheelset intermediate frame) at the wheelset due to the normal contact forces on the treads can be easily identified as the third and fourth components of $\mathbf{Q}^{nor,wi}_{tread}$, as follows:

$$\begin{aligned} \mathbf{Q}^{nor,wi}_{tread} &= -\left(\mathbf{C}^{clu,wi}_{\mathbf{q}}\right)^T \boldsymbol{\lambda}^{wi} \\ \bar{F}_z^{wi} = \mathbf{Q}^{nor,wi}_{tread}&(3), \quad \hat{M}_x^{wi} = \mathbf{Q}^{nor,wi}_{tread}(4). \end{aligned} \tag{30}$$

This is clear due to the physical interpretation of the reaction forces. These force and torque are due to the normal contact forces at the left tread $F^{nor,wi}_{ltread}$ and the right tread $F^{nor,wi}_{rtread}$ as shown by Fig. 9. The direction of these forces $\overrightarrow{n}_{ltread}$ and $\overrightarrow{n}_{rtread}$ are the normal vectors to the wheel surfaces that are stored in the lookup table since they only depend on the lateral displacement and the irregularity. A simple force and torque balance allows to write a set of two linear algebraic equations that can be used to find the normal contact forces at the treads each time step. Input data are the reaction force and torque, that appear as independent terms, and the contact geometry (position of contact points and normal to the wheels at these points), that appear in the coefficient matrix and can be extracted from the contact lookup table, as follows:

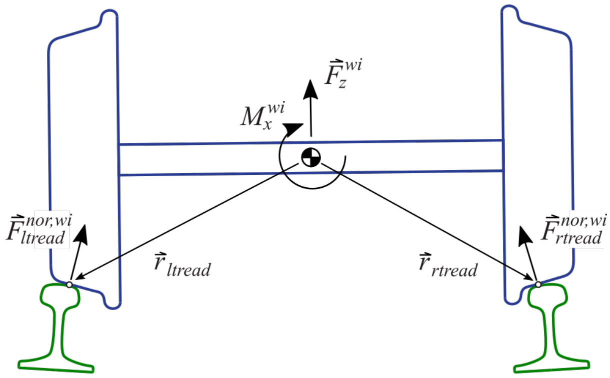

Fig. 9: Forces and torque on wheelset.

$$\begin{bmatrix} \left(\bar{\mathbf{n}}_{ltread}\right)_z & \left(\bar{\mathbf{n}}_{rtread}\right)_z \\ \\ (\hat{\mathbf{r}}_{ltread} \times \hat{\mathbf{n}}_{ltread})_x & (\hat{\mathbf{r}}_{rtread} \times \hat{\mathbf{n}}_{rtread})_x \end{bmatrix} \begin{bmatrix} F_{ltread}^{nor,wi} \\ \\ F_{rtread}^{nor,wi} \end{bmatrix} = \begin{bmatrix} \bar{F}_z^{wi} \\ \\ \hat{M}_x^{wi} \end{bmatrix} \tag{31}$$

Once the location of the contact points and the normal contact forces at the tread and the flange of the wheels are known, the generalised tangential forces $\mathbf{Q}^{tang}$ at these points can be computed. In this investigation, Polach method is used [37] because of its good balance between accuracy and simplicity. To this end, the relative velocity of the contact points on the wheels with respect to the contact points on the rails have to be calculated. These velocities are divided by the wheelset forward velocity to find the so-called creepages. Polach method uses the Kalker's linear coefficients. These coefficients depend on the material properties of the wheel and rail, the curvatures of the surfaces at the contact points and the normal contact force. The curvatures and the normal contact forces are used to find the semi-axis of the contact ellipse (Hertz theory is assumed to be valid). If the wheel and rail profiles are assumed to be new, as in the examples presented in Sect. 6, the curvatures are piece-wise constant functions that are smoothed to avoid discontinuities. If the profiles are assumed to be worn, the curvatures are calculated using numerical differentiation of the geometry evaluated at the nodal points and possibly using numerical filtering to avoid high frequency space-oscillations of the output. Kalker's linear coefficients cannot be precomputed because the value of the normal contact forces is not known in the pre-processing stage. The strategy followed in this research is to pre-compute the Kalker's linear coefficients for each wheel-rail contact geometry used in the lookup table for a normal contact force equal to one. These "unit-force Kalker's linear coefficients" are stored in the lookup table such that the calculation of the actual ones is very simply obtained online.

4. Wheel-rail contact simulation with KEC profiles

This section presents the use of KEC profiles for the simulation of railway vehicles using relative body-track frame coordinates.

4.1. KEC profiles

The KEC profile associated with the wheel-rail profiles combination has the property that, when contacting ideal railheads with zero width, results in a wheelset with the same space of allowable motion than the wheelset with the real wheel-rail profiles combination. All details about this method can be seen in [26, 35]. Figure 10 on the left shows two wheelsets contacting rails. The sketch on the top with the real wheel-rail profiles combination while the sketch below with the KEC profile. The subspace of allowable motion is characterised by the functions $z^{wi} = z_{clt}(y^{wi})$, $\varphi^{wi} = \varphi_{clt}(y^{wi})$, that are plot on the right-upper part of the figure. The real and KEC wheel profiles are shown in the right-lower part of the figure.

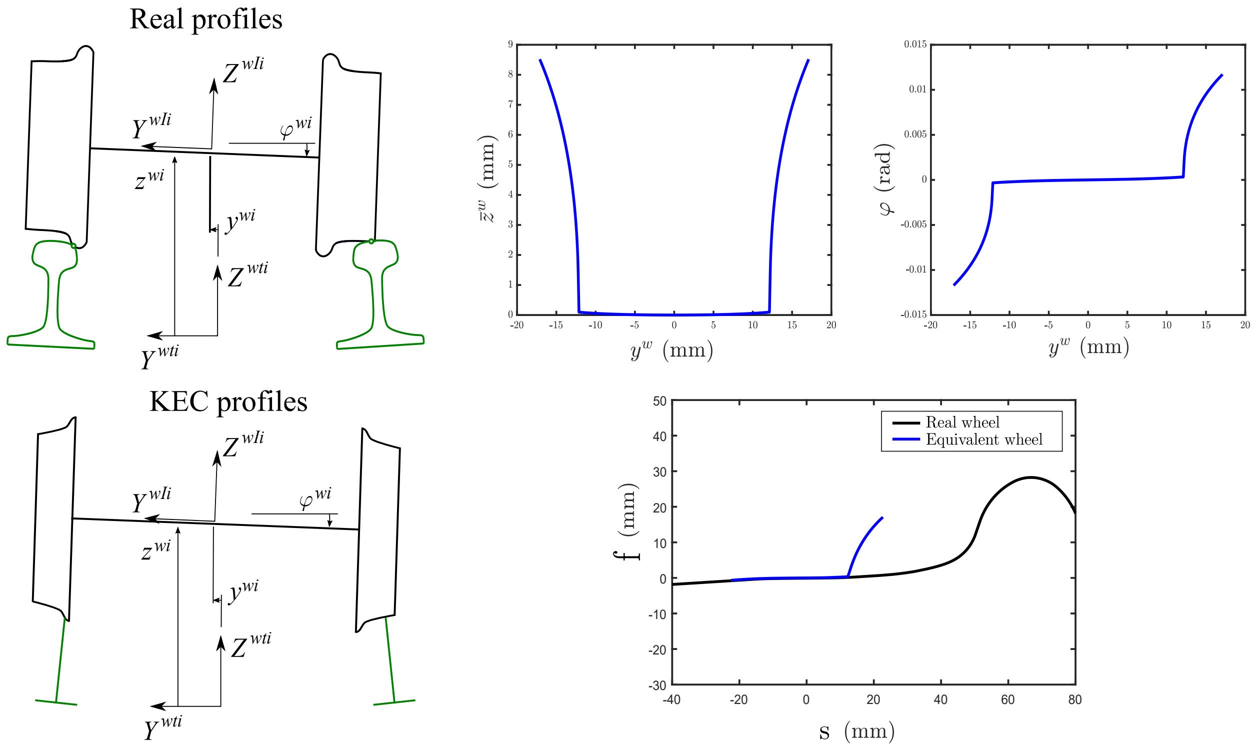

Fig. 10: Real profile and KEC wheel profile.

The contact constraint equations of a wheelset with KEC profiles have a simple form compared with Eq. (17): (a) only the condition of the coincidence of two points belonging to the two surfaces has to be fulfilled, (b) the orthogonality condition for the normal and tangential vectors of two contact surfaces is not needed [26]. Thus, these equations are given by:

$$\mathbf{C}^{KEC,wi}(\mathbf{q}^{wi},\mathbf{s}^{k}) = \begin{bmatrix} 0 & r_0 + f^{lk} & 1 & 0 \\ 0 & r_0 + f^{rk} & 0 & 1 \\ 1 & L_w & \varphi^{wi} & 0 \\ 1 & -L_w & 0 & \varphi^{wi} \end{bmatrix} \begin{bmatrix} \bar{z}^{wi} \\ \varphi^{wi} \\ s^{lk} \\ s^{rk} \end{bmatrix} - \begin{bmatrix} y^{wi} - y^{lir} \\ y^{wi} - y^{rir} \\ -f^{lk} - z^{lir} \\ -f^{rk} - z^{rir} \end{bmatrix} \tag{32}$$

where $\mathbf{s}^k = \begin{bmatrix} s^{lk} & s^{rk} \end{bmatrix}^T$ are the lateral positions of the contact point in the left and right KEC profiles, f^{lk} and f^{rk} are the value of the equivalent profiles at these locations and r_0 is the rolling radius of the wheel when centered in the track. The main advantage of the use of KEC profiles instead of the real ones are [26, 35]:

1. Contact forces on the tread and the flange are treated equally (avoiding hybrid methods).
2. Contact constraints can be solved online keeping a good computational efficiency.
3. Wheel climbing can be simulated.
4. Two-point contact scenario can be simulated with a smooth transition of the normal contact forces from tread to flange.

Regarding the simulation of wheel climbing, some authors claim that the lead-lag contact may have important influence on this phenomenon. Lead-lag contact cannot be simulated with the KEC-method. However, recent work and the author's experience [27] shows that this influence of the lead-lag contact may not be that important.

4.2. Equivalence of lookup tables and KEC-method in irregular tracks

In the KEC-method, the computation of the equivalent wheel profiles requires the wheelset kinematics with respect to an ideal track [26]. However, these profiles can be used in irregular tracks with accuracy. This is an advantage with respect to traditional contact lookup tables that need to store the wheelset kinematics and contact solution for tracks with a set of different values of the gauge. This is, the lookup table contact method requires a 2-entry table, while the KEC-method requires a 1-entry table. Nonetheless, the resulting KEC profiles appear to be valid for different values of the gauge, as shown below.

To show this equivalence in irregular tracks, the wheelset kinematics using contact lookup tables and KEC-method is compared next. To that end, a wheelset with wheels S1002 profile and rails LB.140-AREA profile are considered [35]. Figure 11 and Fig. 12 show the wheelset vertical displacement and roll angle coordinate with respect to the track centreline within a range of track gauge variations Δgv of ± 9 mm respectively.

Figure 13 and Fig. 14 show the absolute differences between the contact solution using lookup tables and KEC-method. As shown in both figures, the error obtained for both wheelset vertical displacement and roll angle is bigger the higher the gauge variation is. This outermost case, which is given by a 9-mm track gauge variation, provides a 60 μm vertical distance and a 0.16 mrad errors when the contact point is at the flange before wheel climb. These are quite low errors when compared to the high-order magnitudes given at Fig. 11 and Fig. 12 respectively. Moreover, those differences are almost inappreciable when the contact point lies on the tread. It can be concluded that the KEC-method provides an accurate kinematic solution for its use in tracks with irregularities.

4.3. Calculation of contact forces when using the KEC method

When using the KEC method two main difficulties are found:

1. Normal contact forces cannot be obtained with the classical Lagrange multiplier method.
2. The tangential contact forces cannot be applied on the equivalent profile.

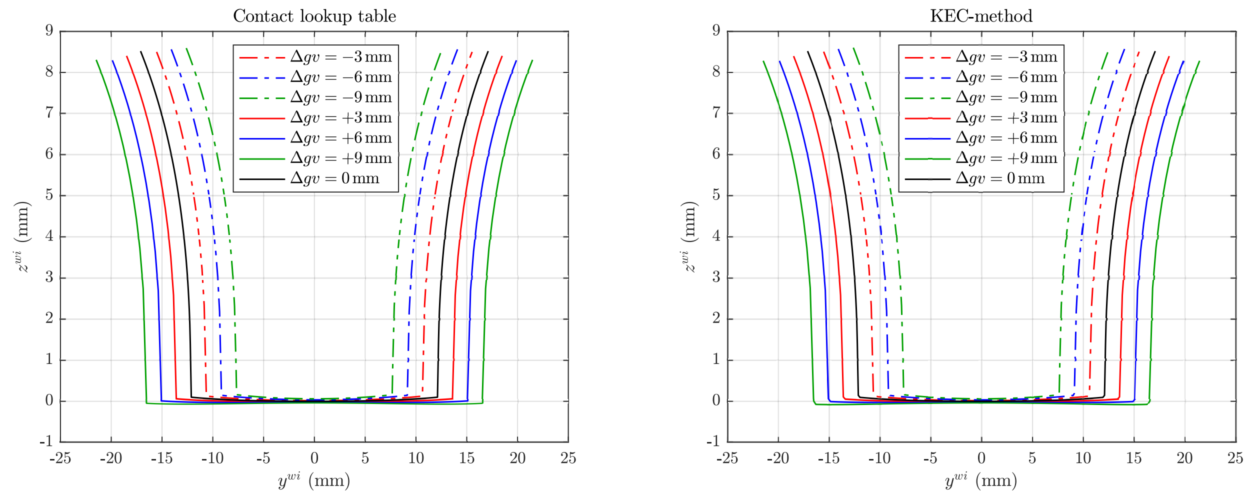

Fig. 11: Wheelset vertical displacement with respect to track centreline for different values of gauge irregularity. Left: contact lookup table. Right: KEC-method.

The second problem has an easy solution. When finding the KEC profile, a table is created to find the position of the contact points in the real profiles once the position of the contact points in the KEC profile is found solving Eq. (32). The solution of the first problem is more involved as explained next. Equation (32) is written in terms of the wheelset coordinates $\mathbf{q}^{wi}$ and the profile parameters $\mathbf{s}^k$. If these profile parameters could be eliminated from Eq. (32), reducing it to a set of two equations and three unknowns (y^{wi}, z^{wi} and φ^{wi}), just like Eq. (20), then the problem would be solved and the Lagrange multipliers method could be used to find the normal contact forces. Unfortunately, the elimination of $\mathbf{s}^k$ is not possible due to the non-linearity of Eq. (32). It can be concluded that, for the KEC-method:

$$\mathbf{Q}^{nor} \neq -\left(\mathbf{C}_{\mathbf{q}}^{KEC}\right)^T \boldsymbol{\lambda}. \tag{33}$$

where the Jacobian matrix $\mathbf{C}_{\mathbf{q}}^{KEC}$ is the result of assembling the Jacobian matrices $\mathbf{C}_{\mathbf{q}}^{KEC,wi}$ associated with all wheelsets in the vehicle.

In the classical method of the Lagrange multipliers, the rows of the Jacobian matrix provide the direction of the reaction forces in the space of the generalised coordinates, while the multipliers mean the number that these rows have to be multiplied by to obtain the generalised reaction forces. In the problem at hand, the Jacobian matrix is not needed to find the direction of the reaction forces, because these directions are known in advance: the normal vectors to the real wheel profiles. Therefore, the reaction forces for wheelset wi can be obtained as:

$$\mathbf{Q}^{nor} = -\begin{bmatrix} \bar{\mathbf{n}}_{lw} & \bar{\mathbf{n}}_{rw} \\ \hat{\mathbf{r}}_{lw} \times \hat{\mathbf{n}}_{lw} & \hat{\mathbf{r}}_{rw} \times \hat{\mathbf{n}}_{rw} \end{bmatrix} \begin{bmatrix} \lambda_{lw}^{wi} \\ \lambda_{rw}^{wi} \end{bmatrix} = -\mathbf{N}^{wi}\boldsymbol{\lambda}^{wi} \tag{34}$$

The coefficient matrix $\mathbf{N}^{wi}$ of this equation looks similar to the one that appear in Eq. (31). However, $\mathbf{N}^{wi}$ includes the complete set vector components (it is 6×2) instead of single components (the

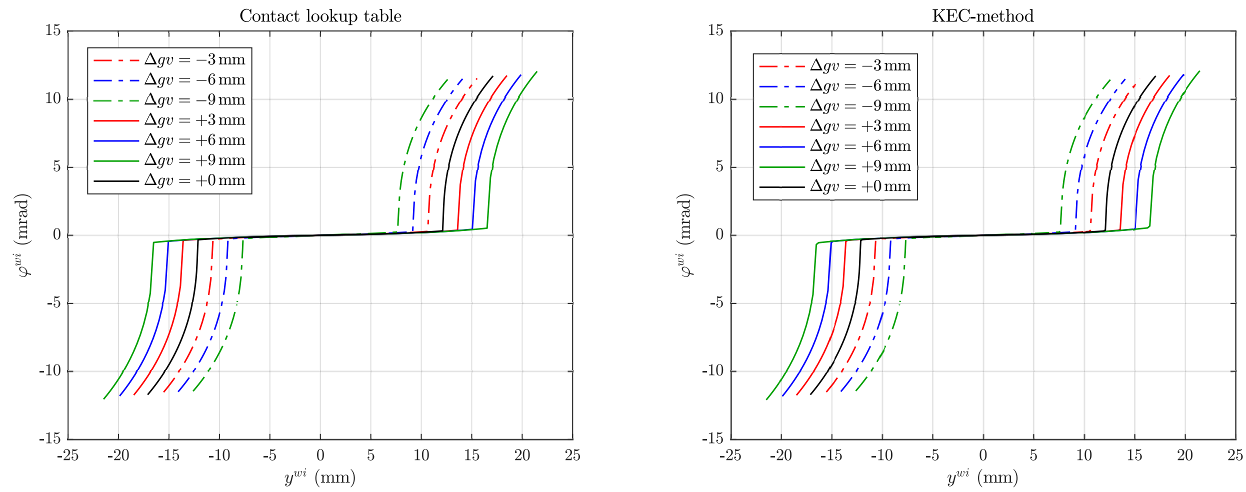

Fig. 12: Wheelset roll angle with respect to track centreline for different values of gauge irregularity. Left: contact lookup table. Right: KEC-method.

one in Eq. (31) is 2×2). An important benefit of this alternative formulation of the Lagrange multipliers method is that the multipliers can be directly identified with the normal contact forces, this is:

$$
\begin{aligned}
F_{lw}^{nor,wi} &= \lambda_{lw}^{wi}, \\
F_{rw}^{nor,wi} &= \lambda_{rw}^{wi}.
\end{aligned}
\tag{35}
$$

Therefore, once the Lagrange multipliers are obtained after solving the equations of motion each time-step, no additional equations, like Eq. (31), have to be solved to find the normal contact forces.

Substituting the reaction forces from Eq. (34) into the equations of motion yields:

$$
\begin{aligned}
&\mathbf{M}\ddot{\mathbf{q}} + \mathbf{N}\boldsymbol{\lambda} = \mathbf{Q} + \mathbf{Q}^{tang} \\
&\mathbf{C}^{KEC} = \mathbf{0}
\end{aligned}
\tag{36}
$$

where $\mathbf{N}$ and $\mathbf{C}^{KEC}$ are the results of assembling the matrices $\mathbf{N}^{wi}$ and the vectors $\mathbf{C}^{KEC,wi}$ associated with all the wheelsets in the vehicle.

Equation (36) represents a system of differential-algebraic equations (DAE). Because the constraints are augmented at position level, this DAE system is called index-3 [41]. It is common in multibody dynamics to substitute the constraint equations by their second time-derivative. In that case the system is called DAE-index 1. In these derivatives, the wheelset accelerations have to be isolated with respect to $\mathbf{s}^k$. In this case, this isolation has no difficulty because the constraint equations at acceleration level are linear. The process starts with the calculation of the first time-derivative of

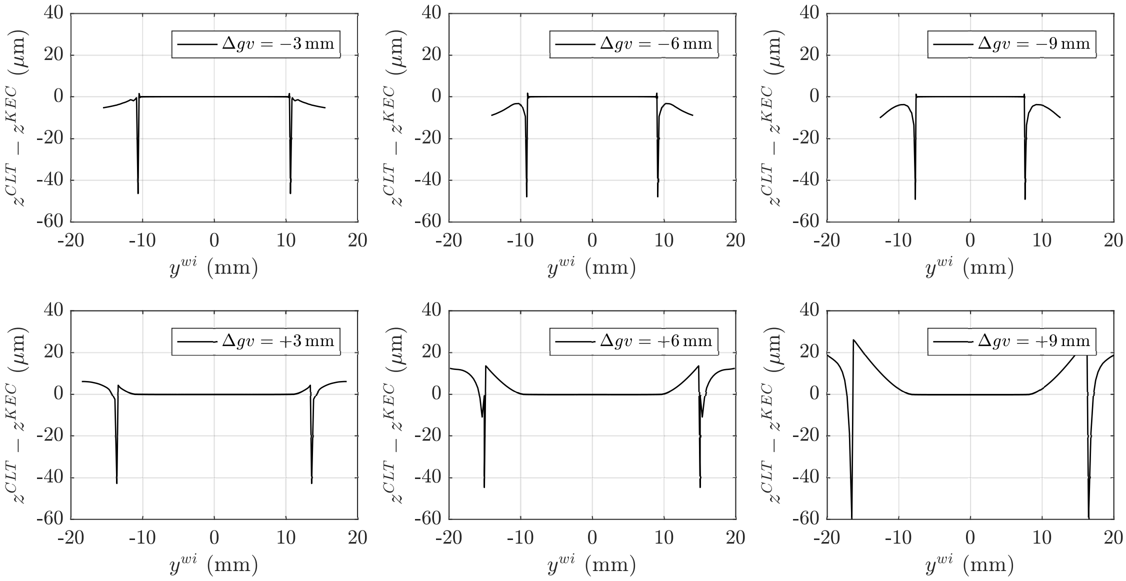

Fig. 13: Absolute differences between contact lookup tables and KEC kinematics in the wheelset vertical displacement with respect to track centreline for different values of gauge irregularity.

the KEC constraints, as follows:

$$\dot{\mathbf{C}}^{KEC,wi} = \frac{\partial \mathbf{C}^{KEC,wi}}{\partial \mathbf{q}^{wi}}\dot{\mathbf{q}}^{wi} + \frac{\partial \mathbf{C}^{KEC,wi}}{\partial \mathbf{s}^{k}}\dot{\mathbf{s}}^{k} + \begin{bmatrix} \dot{y}^{lir} \\ \dot{z}^{lir} \\ \dot{y}^{rir} \\ \dot{z}^{rir} \end{bmatrix} = \mathbf{C}_{\mathbf{q}}^{KEC,wi}\dot{\mathbf{q}}^{wi} + \mathbf{C}_{\mathbf{s}}^{KEC,wi}\dot{\mathbf{s}}^{k} + \dot{\mathbf{x}}^{ir} = \mathbf{0}, \quad (37)$$

where $\mathbf{x}^{ir}$ includes the four track irregularities. The second-time derivative of the constraints are given by:

$$\ddot{\mathbf{C}}^{KEC,wi} = \mathbf{C}_{\mathbf{q}}^{KEC,wi}\ddot{\mathbf{q}}^{wi} + \mathbf{C}_{\mathbf{s}}^{KEC,wi}\ddot{\mathbf{s}}^{k} + \dot{\mathbf{C}}_{\mathbf{q}}^{KEC,wi}\dot{\mathbf{q}}^{wi} + \dot{\mathbf{C}}_{\mathbf{s}}^{KEC,wi}\dot{\mathbf{s}}^{k} + \ddot{\mathbf{x}}^{ir} = \mathbf{0}. \quad (38)$$

The Jacobian matrices $\mathbf{C}_{\mathbf{q}}^{KEC,wi}$ (4×6) and $\mathbf{C}_{\mathbf{s}}^{KEC,wi}$ (4×2) can be separated into two submatrices with two rows each, as follows:

$$\mathbf{C}_{\mathbf{q}}^{KEC,wi} = \begin{bmatrix} \mathbf{C}_{\mathbf{q}}^{a} \\ \mathbf{C}_{\mathbf{q}}^{b} \end{bmatrix}, \quad \mathbf{C}_{\mathbf{s}}^{KEC,wi} = \begin{bmatrix} \mathbf{C}_{\mathbf{s}}^{a} \\ \mathbf{C}_{\mathbf{s}}^{b} \end{bmatrix}. \quad (39)$$

Accordingly, the second time-derivative of the constraints given in Eq. (38) can be separated into two vectors with two rows:

$$\ddot{\mathbf{C}}^{a} = \mathbf{C}_{\mathbf{q}}^{a}\ddot{\mathbf{q}}^{wi} + \mathbf{C}_{\mathbf{s}}^{a}\ddot{\mathbf{s}}^{k} + \dot{\mathbf{C}}_{\mathbf{q}}^{a}\dot{\mathbf{q}}^{wi} + \dot{\mathbf{C}}_{\mathbf{s}}^{a}\dot{\mathbf{s}}^{k} + (\ddot{\mathbf{x}}^{ir})^{a} = \mathbf{0}. \quad (40a)$$

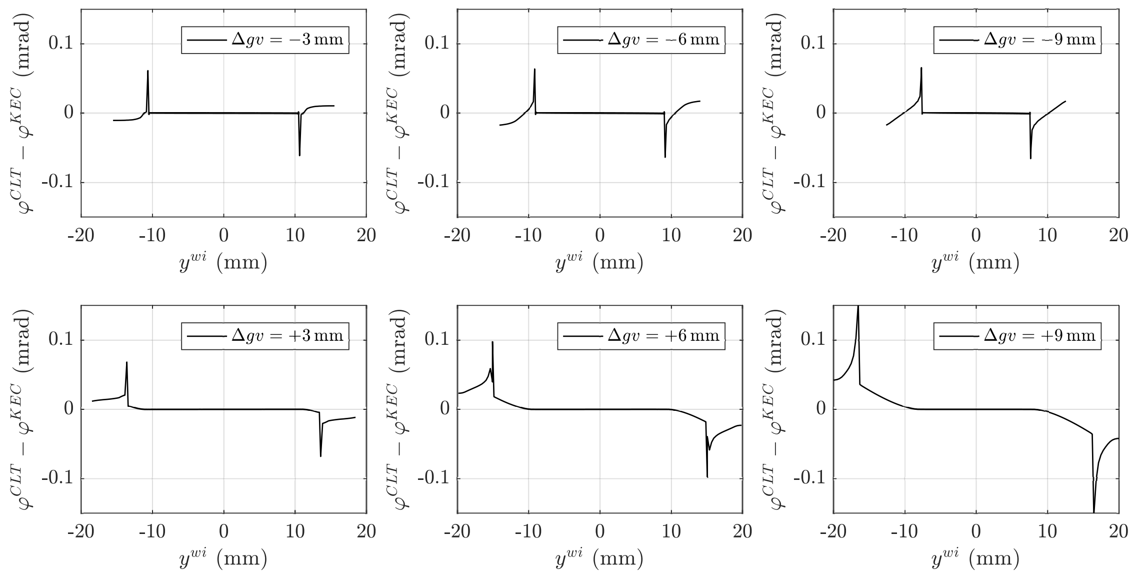

Fig. 14: Absolute differences between contact lookup tables and KEC kinematics in the wheelset roll angle with respect to track centreline for different values of gauge irregularity.

$$\ddot{\mathbf{C}}^b = \mathbf{C}^b_{\mathbf{q}}\ddot{\mathbf{q}}^{wi} + \mathbf{C}^b_{\mathbf{s}}\ddot{\mathbf{s}}^k + \dot{\mathbf{C}}^b_{\mathbf{q}}\dot{\mathbf{q}}^{wi} + \dot{\mathbf{C}}^b_{\mathbf{s}}\dot{\mathbf{s}}^k + (\ddot{\mathbf{x}}^{ir})^b = \mathbf{0}. \tag{40b}$$

The second time-derivative of the constraints of Eq. (40b) can be manipulated to isolate $\ddot{s}^k$, as follows:

$$\begin{aligned}
&\mathbf{C}^b_{\mathbf{q}}\ddot{\mathbf{q}}^{wi} + \mathbf{C}^b_{\mathbf{s}}\ddot{\mathbf{s}}^k = -\dot{\mathbf{C}}^b_{\mathbf{q}}\dot{\mathbf{q}}^{wi} - \dot{\mathbf{C}}^b_{\mathbf{s}}\dot{\mathbf{s}}^k - (\ddot{\mathbf{x}}^{ir})^b \Rightarrow \\
&\Rightarrow \ddot{\mathbf{s}}^k = -(\mathbf{C}^b_{\mathbf{s}})^{-1}\left[\mathbf{C}^b_{\mathbf{q}}\ddot{\mathbf{q}}^{wi} + \dot{\mathbf{C}}^b_{\mathbf{q}} + \dot{\mathbf{C}}^b_{\mathbf{s}}\dot{\mathbf{s}}^k + (\ddot{\mathbf{x}}^{ir})^b\right]
\end{aligned} \tag{41}$$

Substituting Eq. (41) into Eq. (40a), one gets:

$$\begin{aligned}
&\mathbf{C}^a_{\mathbf{q}}\ddot{\mathbf{q}}^{wi} - \mathbf{C}^a_{\mathbf{s}}(\mathbf{C}^b_{\mathbf{s}})^{-1}\left[\mathbf{C}^b_{\mathbf{q}}\ddot{\mathbf{q}}^{wi} + \dot{\mathbf{C}}^b_{\mathbf{q}}\dot{\mathbf{q}}^{wi} + \dot{\mathbf{C}}^b_{\mathbf{s}}\dot{\mathbf{s}}^k + (\ddot{\mathbf{x}}^{ir})^b\right] = -\dot{\mathbf{C}}^a_{\mathbf{q}}\dot{\mathbf{q}}^{wi} - \dot{\mathbf{C}}^a_{\mathbf{s}}\dot{\mathbf{s}}^k - (\ddot{\mathbf{x}}^{ir})^a \Rightarrow \\
&\Rightarrow \left(\mathbf{C}^a_{\mathbf{q}} - \mathbf{C}^a_{\mathbf{s}}(\mathbf{C}^b_{\mathbf{s}})^{-1}\mathbf{C}^b_{\mathbf{q}}\right)\ddot{\mathbf{q}}^{wi} = \\
&= -(\ddot{\mathbf{x}}^{ir})^a - \mathbf{C}^a_{\mathbf{s}}(\mathbf{C}^b_{\mathbf{s}})^{-1}(\ddot{\mathbf{x}}^{ir})^b - \left(\dot{\mathbf{C}}^a_{\mathbf{q}} - \mathbf{C}^a_{\mathbf{s}}(\mathbf{C}^b_{\mathbf{s}})^{-1}\dot{\mathbf{C}}^b_{\mathbf{q}}\right)\dot{\mathbf{q}}^{wi} - \left(\dot{\mathbf{C}}^a_{\mathbf{s}} - \mathbf{C}^a_{\mathbf{s}}(\mathbf{C}^b_{\mathbf{s}})^{-1}\dot{\mathbf{C}}^b_{\mathbf{s}}\right)\dot{\mathbf{s}}^k
\end{aligned} \tag{42}$$

These are two constraint equations in which $\ddot{\mathbf{s}}^k$ does not appear. They can be augmented to the generalised force balance in the equations of motion. This equation can be written with a simplified notation as follows:

$$\mathbf{B}^{wi}\ddot{\mathbf{q}}^{wi} = -\mathbf{D}^{wi}_{ir} - \mathbf{E}^{wi}\dot{\mathbf{q}}^{wi} - \mathbf{G}^{wi}\dot{\mathbf{s}}^k, \tag{43}$$

where

$$\begin{aligned}
\mathbf{B}^{wi} &= \mathbf{C}^a_{\mathbf{q}} - \mathbf{C}^a_{\mathbf{s}}(\mathbf{C}^b_{\mathbf{s}})^{-1}\mathbf{C}^b_{\mathbf{q}}, \\
\mathbf{D}^{wi}_{ir} &= -(\ddot{\mathbf{x}}^{ir})^a - \mathbf{C}^a_{\mathbf{s}}(\mathbf{C}^b_{\mathbf{s}})^{-1}(\ddot{\mathbf{x}}^{ir})^b, \\
\mathbf{E}^{wi} &= \dot{\mathbf{C}}^a_{\mathbf{q}} - \mathbf{C}^a_{\mathbf{s}}(\mathbf{C}^b_{\mathbf{s}})^{-1}\dot{\mathbf{C}}^b_{\mathbf{q}}, \\
\mathbf{G}^{wi} &= \dot{\mathbf{C}}^a_{\mathbf{s}} - \mathbf{C}^a_{\mathbf{s}}(\mathbf{C}^b_{\mathbf{s}})^{-1}\dot{\mathbf{C}}^b_{\mathbf{s}}.
\end{aligned} \tag{44}$$

The term $\mathbf{D}^{wi}_{ir}$ is linear with respect to the second time-derivative of the irregularities. This term has little influence because the relatively high-wave length irregularities that are considered in rigid-body railway dynamics vary smoothly. In addition, it is a term that in practice is difficult to know accurately. Therefore, this term will be neglected in the following.

Considering all the developments shown in this chapter, the equations of motion of the railway vehicle of Eq. (36) can also be written in the following DAE-index 1 form:

$$\begin{bmatrix} \mathbf{M} & \mathbf{N} \\ \mathbf{B} & \mathbf{0} \end{bmatrix} \begin{bmatrix} \ddot{\mathbf{q}} \\ \boldsymbol{\lambda} \end{bmatrix} = \begin{bmatrix} \mathbf{Q} + \mathbf{Q}^{tang} \\ -\mathbf{E}\dot{\mathbf{q}} - \mathbf{G}\dot{\mathbf{s}} \end{bmatrix} \tag{45}$$

where $\mathbf{N}$, $\mathbf{B}$, $\mathbf{E}$ and $\mathbf{G}$ are the result of assembling the matrices $\mathbf{N}^{wi}$, $\mathbf{B}^{wi}$, $\mathbf{E}^{wi}$ and $\mathbf{G}^{wi}$ associated with all the wheelsets in the vehicle. Vector $\dot{\mathbf{s}}$ includes the profile parameters $\dot{\mathbf{s}}^k$ of all the wheelsets in the vehicle. To find the value of $\dot{\mathbf{s}}^k$, the first derivative of the constraint equations given in Eq. (37) has to be solved each time-step. This is a linear algebraic system of 4 equations and 2 unknowns. If the coordinates fulfil the KEC equations, the resulting linear system has to be compatible and it can be solved using the pseudo-inverse.

The calculation of the generalised tangential forces $\mathbf{Q}^{tang}$ follows the same procedure that was explained in Section 3.3.

5. Generation of lookup tables for flanging wheelsets

For the generation of contact lookup tables of wheelsets with wheel-rail profiles combination that show 2-point contact, this is, simultaneous contact in the tread and the flange, the procedure differs depending on whether these tables are going to be used with a hybrid method (explained in Section 3) or with a KEC-method (explained in Section 4). Recall that the KEC-method is an online contact method that requires the real wheel-rail contact problem to be solved first to find the equivalent profiles. In this context, Fig. 15 illustrates such difference between methods.

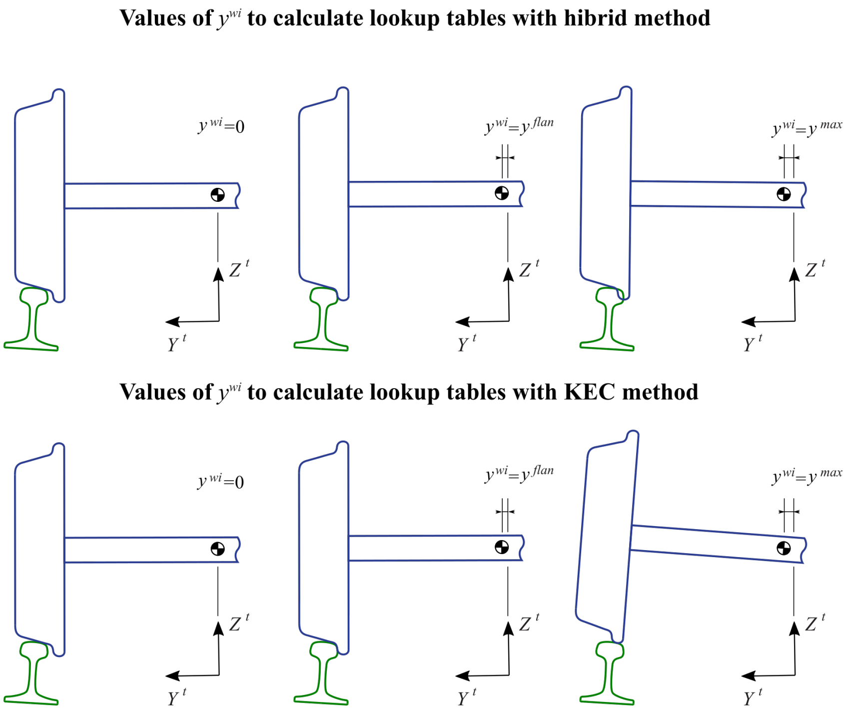

Fig. 15: Lateral displacement of wheels in the generation of lookup tables.

Assume that, for the track with nominal gauge, the lateral displacement that produces 2-point contact is y^{flan}. Then, the range of values of y^{wi} for which the lookup table is calculated is $\begin{bmatrix} 0 & y^{max} \end{bmatrix}$, being $y^{max} > y^{flan}$. In the sub-range $y^{wi} \in \begin{bmatrix} 0 & y^{flan} \end{bmatrix}$ the lookup tables for both methods are equal. However, in the sub-range $y^{wi} \in \begin{bmatrix} y^{flan} & y^{max} \end{bmatrix}$ the lookup table for both methods differs.

In the case of lookup tables to be used with a hybrid method, the constraint contact on the tread is kept, allowing the wheel flange to penetrate the railhead. The location of the point of maximum indentation is stored in the lookup table to be used online as the flange contact point. In the case of the KEC-method, the constraint contact is moved to the flange, allowing the wheel tread to separate the railhead [35]. That way, the KEC-method accounts for the wheel climbing that is fundamental in simulation of derailment.

6. Simulation results

In this section, to analyse the differences between the lookup table and the KEC-method, a numerical comparison of three different case studies is presented: (1) simulation in irregular track with a wheel-rail profile combination that does not show 2-point contact, (2) simulation in irregular track with a wheel-rail profile combination that shows 2-point contact and (3) a wheelset climbing and derailment scenario with a wheel-rail profile combination that shows 2-point contact. The contact lookup tables for the different wheel-rail combinations are discretized for 11 different track gauge irregularities and a range of 350-400 different wheelset lateral displacements, which results in a storage size of around 25 KB for each case. Also, the variable-time step integrator *ode15s* with relative and absolute tolerances of $1 \cdot 10^{-6}$ and a maximum time step of $\Delta t = 1$ ms is used for the dynamic simulations described in the rest of the paper.

Tab. 1: Simulation parameters for the vehicle

Wheelsets	Parameters	Bogie	Parameters
Mass m^{wh}	1568 kg	Mass m^{b}	2982 kg
Roll inertia I_{xx}^{wh}	656 kg·m^2	Roll inertia I_{xx}^{b}	1398.5 kg·m^2
Pitch inertia I_{yy}^{wh}	168 kg·m^2	Pitch inertia I_{yy}^{b}	2667 kg·m^2
Yaw inertia I_{zz}^{wh}	656 kg·m^2	Yaw inertia I_{zz}^{b}	2667 kg·m^2

For all cases, a three-body suspended vehicle formed by two wheelsets and a bogie frame is analysed. The mass, inertia properties with respect to the wheelset and bogie frame are presented in Table 1. The primary suspension is modelled with four three-dimensional spring-damper elements per wheel depicted in Fig. 16. These elements, that connect the axlebox to the bogie frame, have stiffness and damping properties defined in lateral, vertical and longitudinal direction as shown in Table 2. In this work, axleboxes are assumed to follow the wheelset motion with the exception of the rolling motion. In other words, the body frame of the axle boxed is assumed to be parallel to the wheelset intermediate-frame. Moreover, Polach rolling contact theory [42] is used for tangential contact force computation.

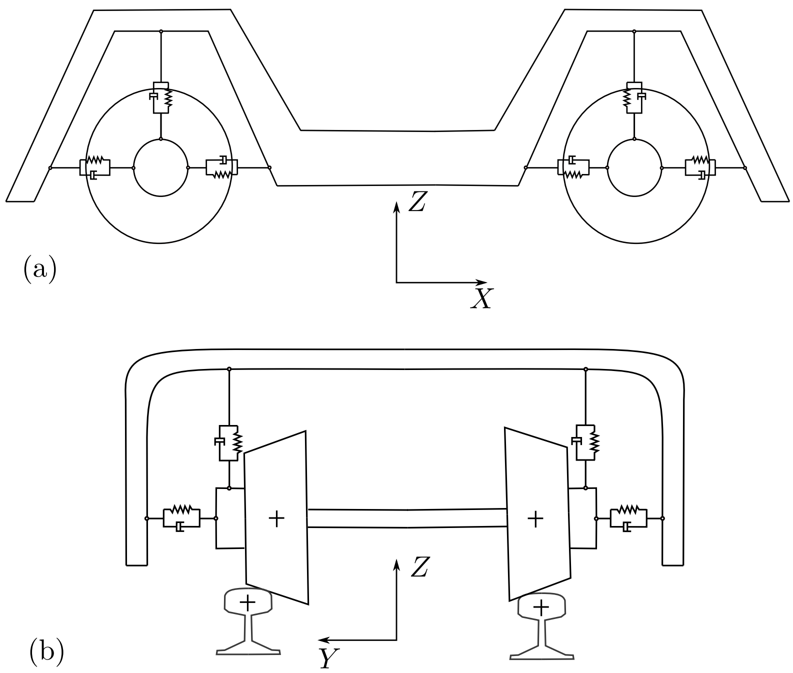

Fig. 16: Three-dimensional vehicle (a) elevation; (b) end view.

Track irregularities are generated using analytical expressions of the power spectral density functions (PSD) [43]. The alignment, vertical profile, gauge variation and cross level are shown in Fig. 17.

Tab. 2: Primary suspension element used in the vehicle

Suspension element direction	Spring stiffness (N/m)	Damping Coeff. (N·s/m)	Number of elements
Lateral	$1.5 \cdot 10^6$	$4.5 \cdot 10^4$	4 per bogie
Vertical	$3 \cdot 10^6$	$6.75 \cdot 10^4$	4 per bogie
Longitudinal	$6 \cdot 10^6$	$9 \cdot 10^4$	8 per bogie

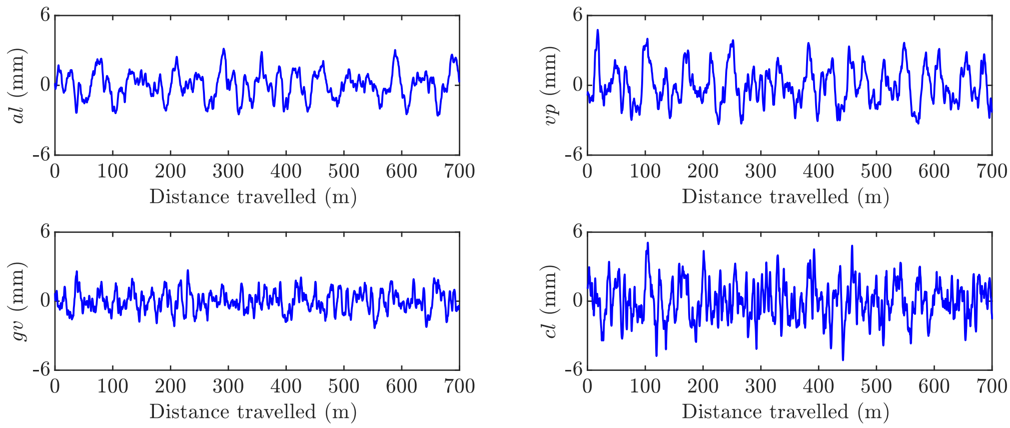

Fig. 17: Track irregularities, *al* is alignment, *vp* is vertical profile, *gv* is gauge variation, *cl* is cross level.

6.1. Simulation results in a track with irregularities with 1-point contact wheel-rail profile combination

The proposed first case study considers a wheel-rail profile combination that does not show 2-point contacts. It is simulated at a constant forward velocity of $V = 10$ m/s, in a 700-m track with irregularities formed by the following five segments: 100-m tangent, 50-m transition, 400-m left curve of $R = 235$ m radius segment, 50-m transition and 100-m tangent. The track geometry is shown in Fig. 18 where the different track segments limits are identified. This segment description is latter used in all simulation results figures. Wheel and rail profiles are shown in Fig. 19, which are those used by the metropolitan train at the city of Seville. The parameters for both the wheelset and the rail are given in Table 3.

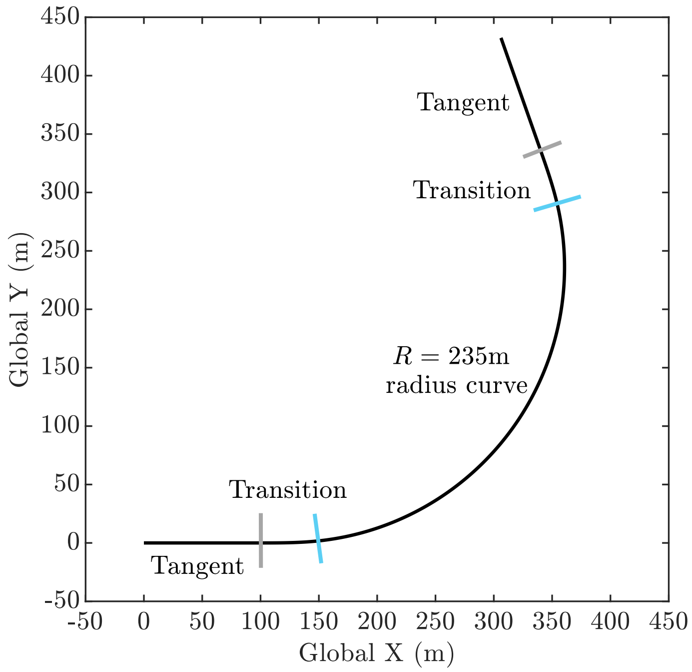

Fig. 18: Track geometry in solid dark line. Lines perpendicular to the track geometry show the transition points of the track segments.

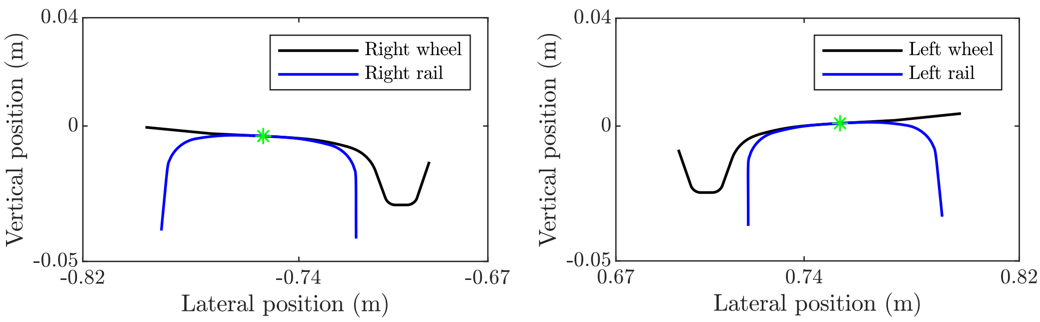

Fig. 19: Wheel-rail profile combination which does not show two point contacts (used by the metropolitan train of the city of Seville).

Tab. 3: Simulation parameters for the wheelset which do not show 2-point contact

Parameters	Model	Parameters	Model	Parameters	Model	Parameters	Model
L_w (m)	0.7526	R_0 (m)	0.43	L_r (m)	0.7526	β (rad)	0.05

The relationship of transverse curve parameters between KEC and real wheel profiles can be found in Fig. 20. It can be seen that for each value of the equivalent parameter s^{lk}, only one contact point in the real profile s^{lw} can be obtained. This corresponds to a single point wheel-rail contact scenario.

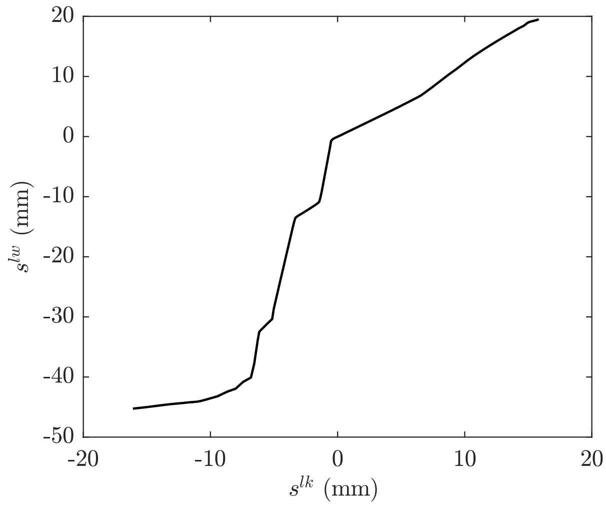

Fig. 20: Transverse curve parameters relation between KEC and real wheel profiles.

The comparison of lateral displacement and yaw angle for the wheelsets and bogie frame using lookup table and KEC-method is shown in Fig. 21. As it can be seen from the figures, the results of both approaches are almost identical. Due to the curve negotiation, the three bodies show negative values of the lateral displacement and the yaw angle. A steady curving motion is not achieved due to the track irregularities.

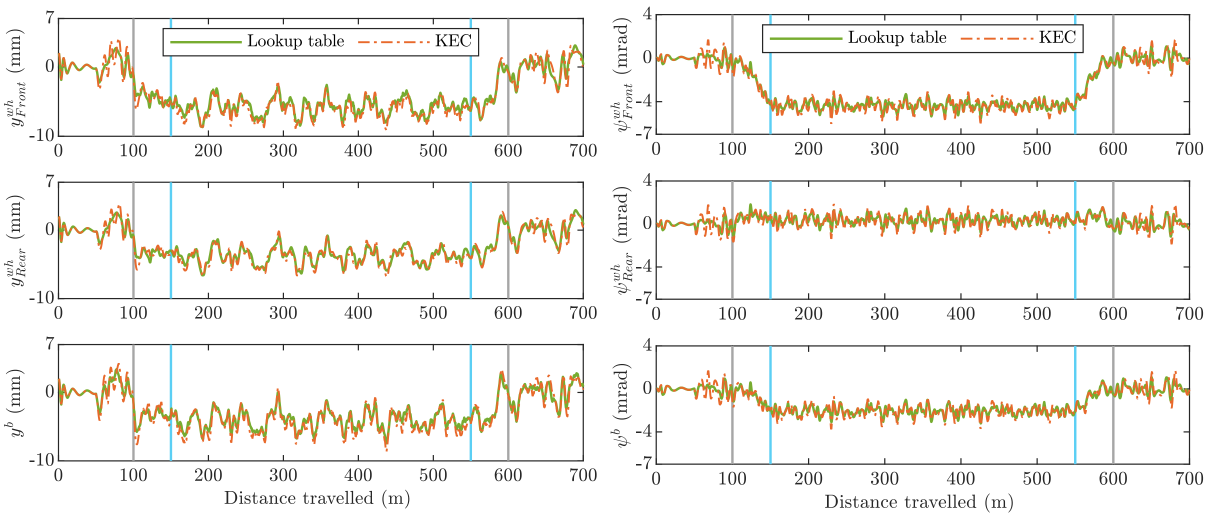

(a) Lateral displacement

(b) Yaw angle

Fig. 21: Comparison of kinematics with the profiles which do not show two-point contact using both approaches. Full vertical lines refer to the limits of track segments as shown in Fig. 18. Top figures show the motion of the front wheelset, middle figures show the motion of the rear wheelset and bottom figures show the motion of the bogie frame.

Figure 22 and Fig. 23 show the comparison of normal contact forces at front and rear wheelsets using both approaches. Since there is always an unique contact point per wheel-rail pair, normal contact forces of both approaches are treated as reaction forces using Eq. (23). In this context, the results from both approaches are very close to each other. When the vehicle negotiates the left curve, right wheel for both wheelsets experiences a higher normal contact force than left one, which has identical behaviour as in [26]. Also note that all constraints used in the paper (for both KEC-method and lookup table method) are bilateral. That means that the associated normal contact force, that is calculated as a reaction force, can be negative (adhesion force). Clearly, these forces would be physically inadmissible. Therefore, simulation results, are acceptable only if the calculated normal contact forces are all compressive.

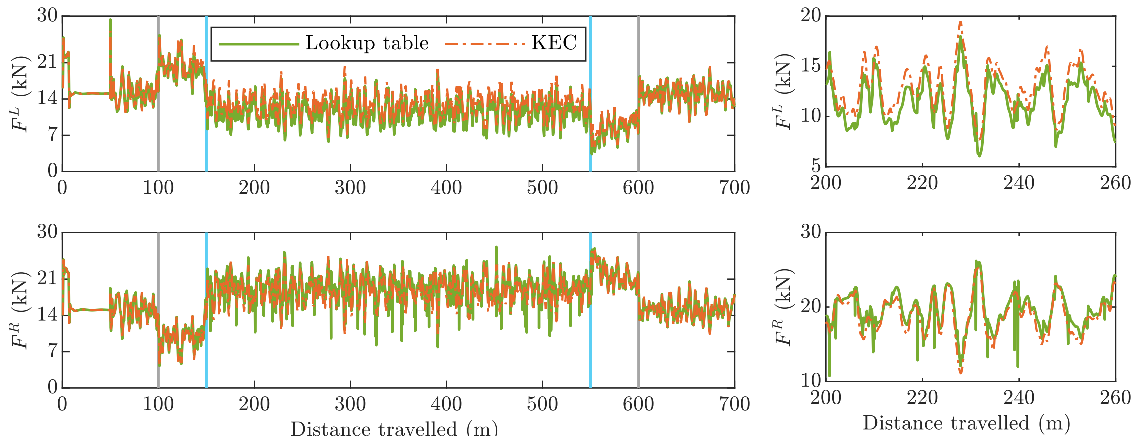

Fig. 22: Comparison of normal contact forces at front wheelset using both approaches. Left: original figure, Right: zoom within the distance travelled from 200 m to 260 m.

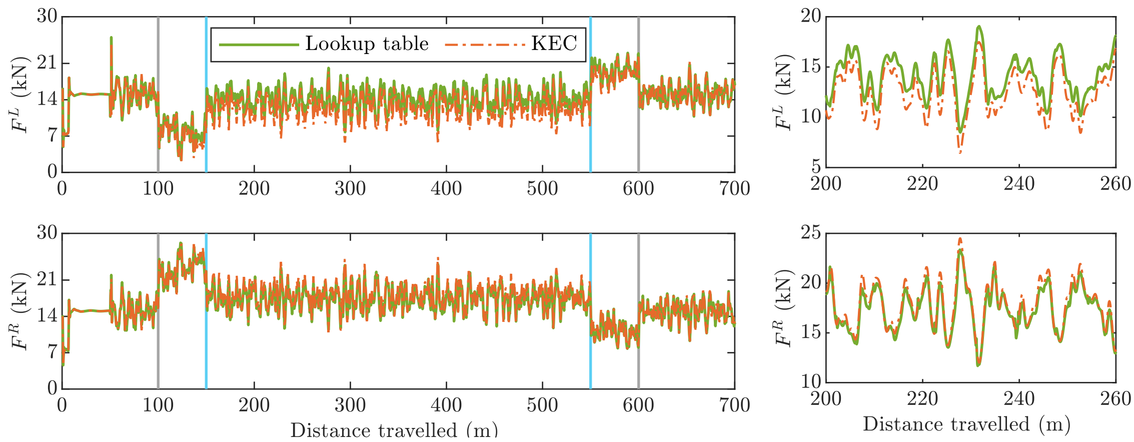

Fig. 23: Comparison of normal contact forces at rear wheelset using both approaches. Left: original figure, Right: zoom within the distance travelled from 200 m to 260 m.

6.2. The selection of the flange contact stiffness with 2-point contact wheel-rail profile combination

The second case study is the same bogie vehicle whose wheelsets use a wheel-rail profile combination that shows two-point contacts. Wheel and rail profiles are shown in Fig. 24. The parameters for the wheelset and the rail are given in Table 4. Moreover, the vehicle is assumed to have a constant forward velocity of $V = 10$ m/s along the same 700-m length track with irregularities shown in Fig. 18.

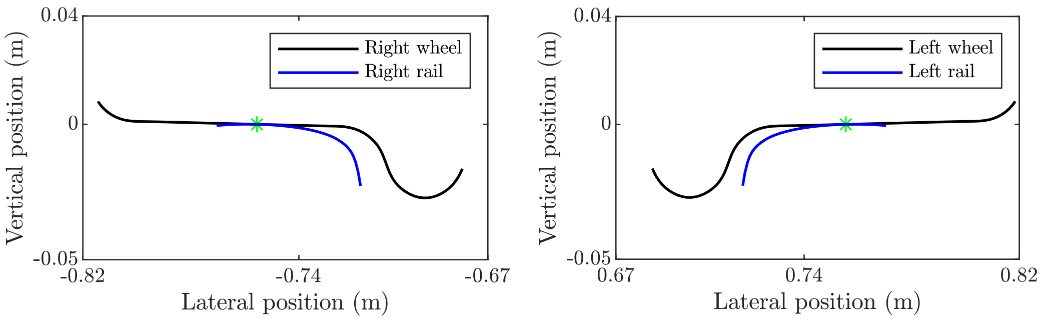

Fig. 24: Wheel-rail profile combination which shows two point contact (S1002 wheel profile and LB-140-Area rail profile).

Tab. 4: Parameters for the wheel-rail profile combination which can show two point contact

Parameters	Model	Parameters	Model	Parameters	Model	Parameters	Model
L_w (m)	0.7515	R_0 (m)	0.457	L_r (m)	0.7555	β (rad)	0

For this case study in which two-point wheel-rail contact scenarios occur, there is an important parameter that controls the simulations using the lookup table method and hybrid contact. This parameter is the flange contact stiffness. According to the wheel-rail profile combination shown in Fig. 24, the Hertzian stiffness at the flange contact point can be computed from the application of the Hertz contact theory in Eq. (29) as $K_{hertz} = 7.7075 \cdot 10^{13}$ N/m$^{1.5}$, where the Poisson's ratio is $\nu = 0.28$ and Young's modulus is $E_k = 2.1 \cdot 10^{11}$ N/m^2. However, the value of this Hertzian stiffness is actually higher than the real one, because Hertz theory assumes that both bodies in contact are semi-infinite spaces. This means that the structural flexibility, which is important for the flange when the load is applied transversely, is not considered.

Since the rail and wheel profiles have fast change of curvature from tread contact to flange contact, the computed Hertzian stiffness evolves similarly. However, the surface parameters to rail/wheel at the flange contact points shows almost no difference for different lateral displacement y^{wh}. The flange contact point remains the same with two-point contact scenario and hybrid method. Thus, in this work, constant values are chosen for flange contact stiffness.

Due to the high values of contact stiffness and because flange contact is an event that appears suddenly as an impact, simulations slow down tremendously any time flange contact occurs. In these conditions, the resulting flange normal contact forces are so high that they can be considered as physically inadmissible.

In this context, Tab. 5 shows a comparison of the computational efficiency of the lookup table method with different flange contact stiffness. Along the different stiffness used for the flange contact, the one that is close to $7.075 \cdot 10^{13}$ N/m$^{1.5}$ leads the integrators to stall during the simulation. If the selected contact stiffness is low, simulations are relatively smooth even with multiple flange contacts. For this reason, the dynamicist may be tempted to use low value of the stiffness just to get any simulation results, or to get them in a reasonable period of time, such as $K_{hertz} = 1 \cdot 10^9$ N/m$^{1.5}$. However, the results may show flange to rail-head indentations so large that they can be considered as physically inadmissible as shown in Fig. 25.

Tab. 5: Computation efficiency with different flange contact stiffness and damping parameters by using lookup table approach

K_{hertz} (N/m$^{1.5}$) C_{damp} (N $\cdot$ s/m^2)	$1 \cdot 10^{13}$ $1 \cdot 10^{11}$	$1 \cdot 10^{12}$ $1 \cdot 10^{10}$	$1 \cdot 10^{11}$ $1 \cdot 10^{9}$	$1 \cdot 10^{10}$ $1 \cdot 10^{8}$	$1 \cdot 10^{9}$ $1 \cdot 10^{7}$
CPU time ratio (s/1s)	Stall	11.8	6.9	2.45	1.09
Function evaluation	Stall	153338	81265	20901	11822

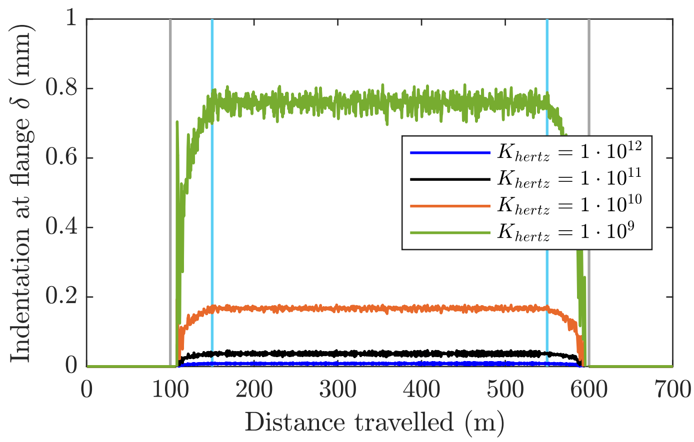

Fig. 25: Flange to rail-head indentations at front wheelsets with different flange contact stiffness when using the lookup table approach. The unit of flange contact stiffness K_{hertz} is N/m$^{1.5}$.

As a conclusion, on the one hand, the selection of the contact stiffness is fundamental in the simulation of wheel flange contact with a hybrid method and, on the other hand, this selection is some-how arbitrary when not much information is known about the local contact process and the wheel structural deformation. In order to improve computation efficiency and obtain physically admissible indentations of the vehicle motion, the Hertzian parameters for the flange contact when using the lookup table approach are chosen as constant values of $K_{hertz} = 1 \cdot 10^{10}$ N/m$^{1.5}$ and $C_{damp} = 1 \cdot 10^8$ N $\cdot$ s/m^2, in the rest of the work.

6.3. Simulation results in a track with irregularities with 2-point contact wheel-rail profile combination

Due to the cumbersome effort to choose flange contact stiffness for the lookup table approach, it is preferable to use a method that treats equally the tread and the flange contacts, as the KEC-method does. The use of the KEC-method results in smooth simulations even with multiple flange contacts. More importantly, the KEC-method is able to simulate wheel climbing. The KEC-method fulfils these conditions. In this and the following sections, the KEC method is compared to the lookup table approach with the two-point contact problem and the wheel-rail profile combination shown in Fig. 24.

Figure 26 plots the location of the contact points in the real profile as a function of the location of the contact point in the KEC profile. It can be seen that for a certain value of the equivalent parameter s^{lk} there are two simultaneous contact points in the real profile s^{lw}. This corresponds to a two-point wheel-rail contact scenario where one contact point is located at the tread s_t^{lw}, and another one is located at the flange s_f^{lw}. Based on the parameters given in [35] to efficiently use the KEC-method with the two-point contact scenario, this relation between the equivalent and real wheel profiles is regularised as a dashed green line in Fig. 26. This allows a continuous contact point evolution from tread to flange avoiding the discontinuities associated with the contact constraints. However, Fig. 26 is not completely used for the lookup table approach, since only tread contact is considered. Instead, an compliant lateral force model is considered to account for wheel penetration at the flange, as shown in Sec. 5.

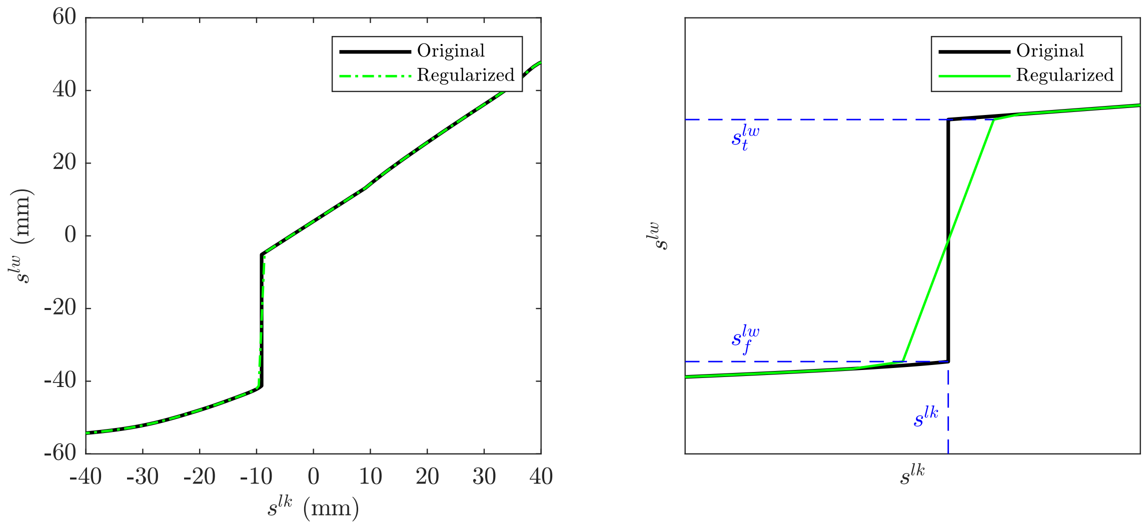

Fig. 26: Regularisation of the transverse curve parameter relation for the left equivalent and real wheels when KEC-method is used.

The vehicle is assumed to have a constant forward velocity of $V = 10$ m/s along the same 700-m length track with irregularities shown in Fig. 18. Due to these rail irregularities, a high frequency content can be observed in the following figures. The lateral displacement and the yaw angle of both wheelsets are compared in Fig. 27. The resulting lateral displacements are quite similar using both approaches. However, when the vehicle enters into the 235 m radius curve, flange contacts occurs. The lateral displacement y^{wh} enters into the sub-range $y^{wh} \in \left[y^{flan} \quad y^{max}\right]$, in which the kinematic of yaw angle for both methods differs (see Fig. 15 in Sec. 5). However, as it can be seen in Fig. 27, the lateral displacement of the vehicle bodies is very similar in this particular problem. Slight differences can be observed in the yaw angles shown in Fig. 27.

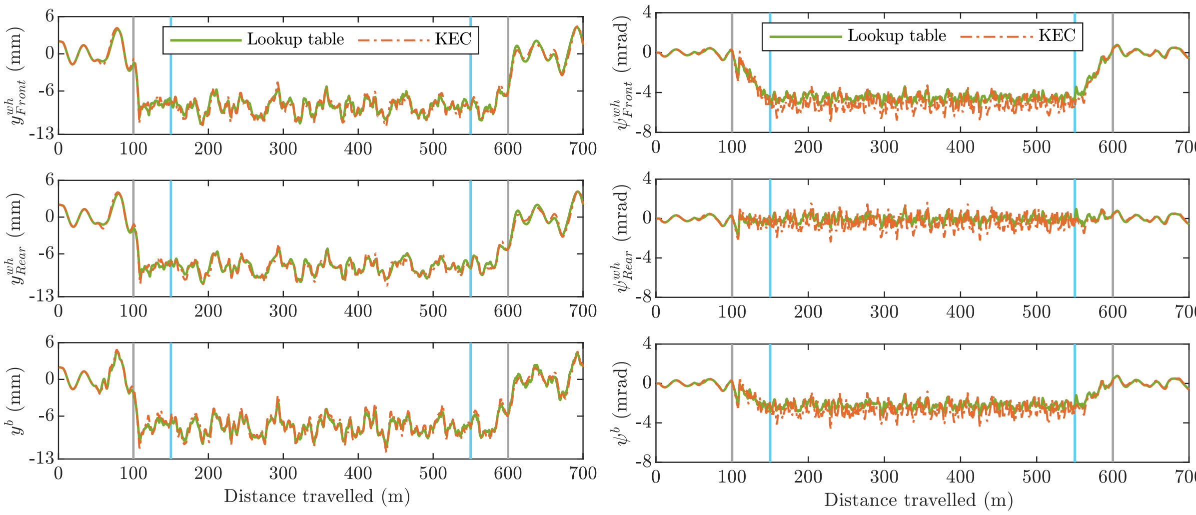

(a) Lateral displacement

(b) Yaw angle

Fig. 27: Comparison of kinematics using profiles that show two-point contacts. Left: lateral displacement, Right: yaw angle.

Figure 28 and Fig. 29 show the comparison of the normal contact force at right wheel of front and rear wheelset using both approaches. The normal contact forces at the right tread and flange differ when the wheelset is negotiating the curve. That is due to the two different contact approaches (constrained in the KEC-method, elastic in the lookup table method) used in the wheel flange area.

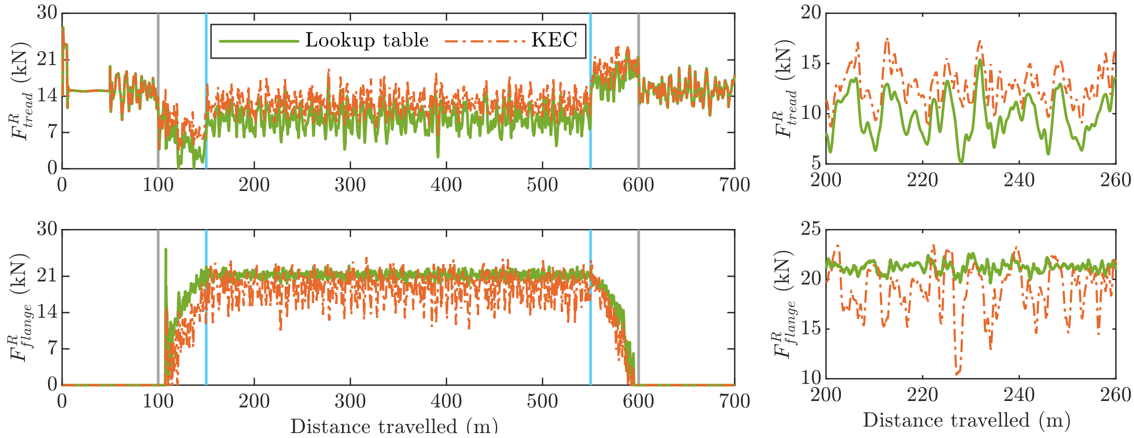

Fig. 28: Comparison of normal contact forces at front wheelset with two-point contacts. Left: original figure, Right: zoom within the distance travelled from 200 m to 260 m.

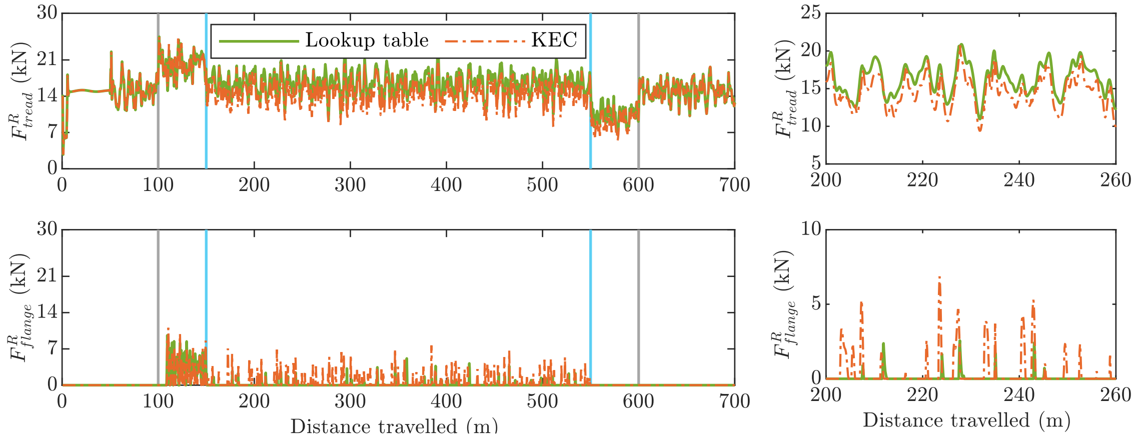

Fig. 29: Comparison of normal contact forces at rear wheelset with two-point contacts. Left: original figure, Right: zoom within the distance travelled from 200 m to 260 m.

6.4. Wheelset climbing and derailment with 2-point contact wheel-rail profile combination

Due to the large angle of attack generated by friction force, wheel climbing and derailment may occur, when the vehicle is running with a high forward velocity or on a small radius curve. In this case study, the bogie vehicle is running at a constant forward velocity of $V = 25$ m/s on a 1000-m track without irregularities, formed by the following five segments: 100-m tangent, 50-m transition, 350-m left curve of R = 100 m radius segment, 150-m transition and 350-m tangent.

The comparison of the lateral and vertical displacement using both approaches is shown in Fig. 30. When using the lookup table approach, the lateral displacement reaches the steady motion due to permanent flange contact. As a result, the vertical displacement keeps constant during the simulation. However, when using the KEC-method, the wheelset vertical displacement at Fig. 30 shows that the wheelset tends to climb several times when it starts to enter into transitions at around 100 m. Due to regularised tread-flange transition used in KEC-method, the rear flange climbs when passing through the small curve and the derailment occurs when the longitudinal coordinate is approximately 380 m.

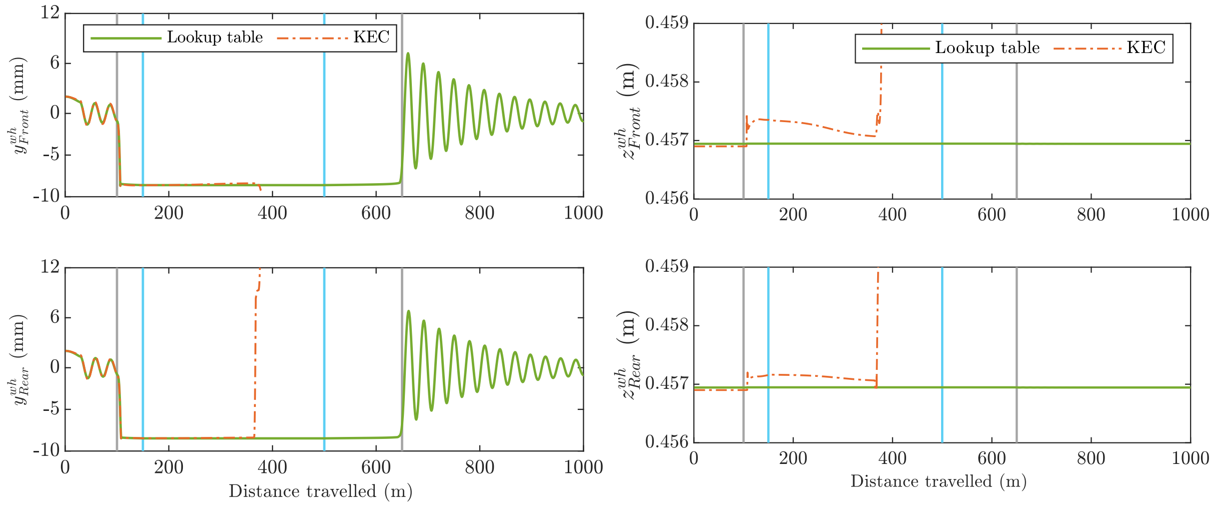

(a) Lateral displacement (b) Vertical displacement

Fig. 30: Comparison of kinematics at wheel-climbing scenario using profiles that show two-point contacts. Left: lateral displacement, Right: vertical displacement.

Finally, Fig. 31 shows the wheelset climbing scenario during the simulation. Accordingly, the configurations of the rear left wheel in the contact point section during the simulation is shown in the same figure with different wheelset lateral displacements. It is observed that the rear left wheel is climbing the rail with one distinct jumps in contact point. The contact point on the wheel tread which is in contact with the top of the rail is jumped to the rail corner, in which wheel flange is in contact. As the lateral displacement increases, the wheel is completely moved up to the top of the rail. This scenario agrees with the results proposed in [30].

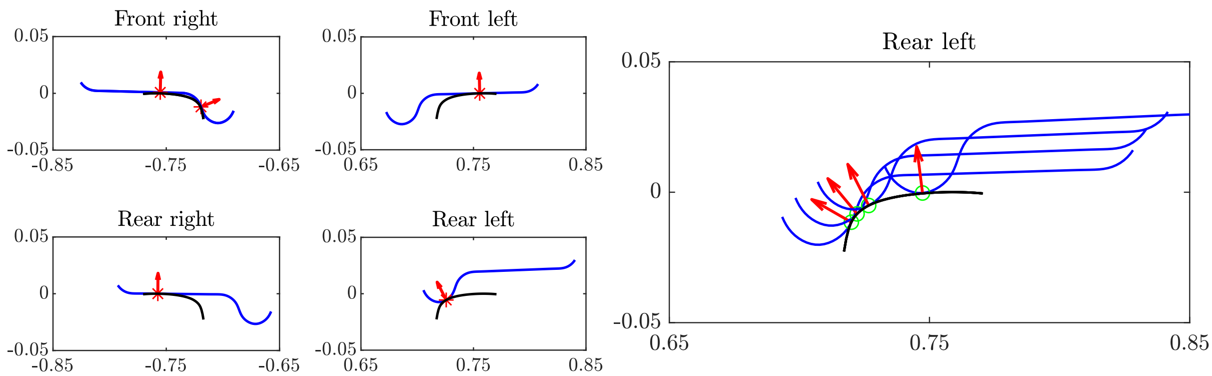

Fig. 31: Frames of the wheelsets during wheelset climbing using KEC approach (Left); Wheel/rail contact in point section with different wheelset lateral displacement during the simulation (Right).

In this example, the lookup method and the KEC-method result in totally different behaviour of the vehicle. As it has been shown, simulations based on the hybrid-lookup table method may produce results that are not in the safe side, because wheel climbing cannot be.

7. Conclusion

Two constraint-based formulations for the wheel-rail contact simulation in multibody dynamics are introduced and compared: the use of precalculated contact lookup tables and the Knife-edge Equivalent Contact method (KEC-method). Contact search simulation with lookup tables is a well-known and widely used technique. This paper describes a method that does not consider the influence of the yaw angle in the contact geometry. This approach, that is sufficiently accurate in most scenarios, is commonly improved in most simulation codes by including the wheelset yaw as an additional entry to the lookup tables. Regarding this method, the original contributions of this paper are: (1) a method for interpolating the tables in the presence of irregularities and (2) a method for the calculation of the normal contact forces that does not require the use of the Jacobian of the wheel-rail contact constraints. This method models the wheel-rail flange contact using an elastic approach to be able to simulate the two-point contact scenario. That is why this method is considered as a hybrid approach.

The KEC-method is a new wheel-rail contact approach recently developed by the authors. The KEC-method substitutes the real wheel and rail profiles with a fictitious wheel profile that contacts a spatial curve such that the relative wheel-track motion remains unchanged. This method results in very important advantages for the simulations: (1) the contact constraints are very simple and can be solved on-line, (2) constraint functions are continuous even in the case of two-point contact, (3) it allows a smooth transition of the contact force from the wheel-tread to the wheel-flange and (4) it is effective in the simulation of wheel climbing. This is the only constraint-based contact method that can be used to simulate the two-point wheel rail contact. Regarding this method, the main contribution of this paper is to show that the wheel KEC profile, that is generated using an irregularity-free track section, remains valid, this is, keeps the same space of allowable motion, also in the presence of track irregularities.

Three different case studies of a bogie vehicle with different wheel-rail profile combinations in a tangent and curved track are examined. Results show that, in general, both approaches provide a similar dynamic behaviour and normal contact forces. Due to the differences in the simulation of flange contact, the wheelsets yaw angle differs at curve negotiation. However, when simulating the negotiation of a curve at relatively high velocity, the results of both methods are drastically different. Due to its ability to simulate wheel climbing, the KEC-method predicts derailment while the lookup-hybrid method predicts a permanent and stable flange contact, even in the presence of track irregularities. It can be concluded that simulations with the lookup-hybrid method may not be on the safe side and the KEC-method can be considered as superior when doing safety analysis.

Acknowledgements

The first and third authors thank the Department of Economy, Science, Enterprise and University of the Andalusian Regional Government, in Spain, under the PAIDI 2020 program with project reference P18-RT-1772. The second author thanks for the support given by Business of Finland under the SmartTram-LUT project with reference 6292/31/2018. All this support is gratefully acknowledged.

Conflicts of interest

The authors declare that there is no conflict of interest to this work.

References

[1] S. Bruni, J. Meijaard, G. Rill, A. Schwab, State-of-the-art and challenges of railway and road vehicle dynamics with multibody dynamics approaches, Multibody Syst Dyn 49 (2020) 1–32.

[2] S. Z. Meymand, A. Keylin, M. Ahmadian, A survey of wheel–rail contact models for rail vehicles, Vehicle System Dynamics 54 (3) (2016) 386–428. doi:10.1080/00423114.2015.1137956.

[3] A. A. Shabana, M. Tobaa, H. Sugiyama, K. E. Zaazaa, On the computer formulations of the wheel/rail contact problem, Nonlinear Dynamics 40 (2) (2005) 169–193. doi:10.1007/s11071-005-5200-y.

[4] Y. Ye, Y. Sun, S. Dongfang, D. Shi, M. Hecht, Optimizing wheel profiles and suspensions for railway vehicles operating on specific lines to reduce wheel wear: a case study, Multibody System Dynamics (2020) 1–32.

[5] P. Antunes, H. Magalhães, J. Ambrosio, J. Pombo, J. Costa, A co-simulation approach to the wheel–rail contact with flexible railway track, Multibody System Dynamics 45 (2) (2019) 245–272.

[6] T. W. Tu, Dynamic modelling of a railway wheelset based on kane's method, International Journal of Heavy Vehicle Systems 27 (1-2) (2020) 202–226.

[7] A. A. Shabana, K. E. Zaazaa, J. L. Escalona, J. R. Sany, Development of elastic force model for wheel/rail contact problems, Journal of Sound and Vibration 269 (1–2) (2004) 295–325. doi:https://doi.org/10.1016/S0022-460X(03)00074-9.

[8] M. Machado, P. Moreira, P. Flores, H. M. Lankarani, Compliant contact force models in multibody dynamics: Evolution of the hertz contact theory, Mechanism and Machine Theory 53 (2012) 99–121.

[9] P. Flores, H. M. Lankarani, Contact force models for multibody dynamics, Vol. 226, Springer, 2016.

[10] A. A. Shabana, J. R. Sany, An augmented formulation for mechanical systems with non-generalized coordinates: application to rigid body contact problems, Nonlinear dynamics 24 (2) (2001) 183–204. doi:10.1023/A:1008362309558.

[11] H. Sugiyama, Y. Suda, On the contact search algorithms for wheel/rail contact problems, Journal of computational and nonlinear dynamics 4 (4).

[12] F. Marques, H. Magalhães, J. Pombo, J. Ambrósio, P. Flores, A three-dimensional approach for contact detection between realistic wheel and rail surfaces for improved railway dynamic analysis, Mechanism and Machine Theory 149 (2020) 103825.

[13] H. Magalhães, F. Marques, B. Liu, P. Antunes, J. Pombo, P. Flores, J. Ambrósio, J. Piotrowski, S. Bruni, Implementation of a non-hertzian contact model for railway dynamic application, Multibody System Dynamics 48 (1) (2020) 41–78.

[14] Y. Sun, W. Zhai, Y. Guo, A robust non-hertzian contact method for wheel–rail normal contact analysis, Vehicle System Dynamics 56 (12) (2018) 1899–1921.

[15] J. Piotrowski, W. Kik, A simplified model of wheel/rail contact mechanics for non-hertzian problems and its application in rail vehicle dynamic simulations, Vehicle System Dynamics 46 (1-2) (2008) 27–48.

[16] Y. Sun, W. Zhai, Y. Ye, L. Zhu, Y. Guo, A simplified model for solving wheel-rail non-hertzian normal contact problem under the influence of yaw angle, International Journal of Mechanical Sciences (2020) 105554.

[17] J. Pombo, J. Ambrósio, M. Silva, A new wheel–rail contact model for railway dynamics, Vehicle System Dynamics 45 (2) (2007) 165–189. doi:https://doi.org/10.1080/00423110600996017.

[18] J. Pombo, J. Ambrósio, Application of a wheel–rail contact model to railway dynamics in small radius curved tracks, Multibody System Dynamics 19 (2008) 91–114. doi:https://doi.org/10.1007/s11044-007-9094-y.

[19] J. Pombo, J. Ambrósio, An alternative method to include track irregularities in railway vehicle dynamic analyses, Nonlinear Dynamics 68 (2012) 161–176. doi:https://doi.org/10.1007/s11071-011-0212-2.

[20] J. J. O'Shea, A. A. Shabana, Analytical and numerical investigation of wheel climb at large angle of attack, Nonlinear Dynamics 83 (2016) 555–577. doi:https://doi.org/10.1007/s11071-015-2347-z.

[21] J. J. O'Shea, A. A. Shabana, Further investigation of wheel climb initiation: Three-point contact, Proceedings of the Institution of Mechanical Engineers, Part K: Journal of Multi-body Dynamics 231 (1) (2017) 121–132.

[22] M. Malvezzi, E. Meli, S. Falomi, A. Rindi, Determination of wheel–rail contact points with semianalytic methods, Multibody System Dynamics 20 (4) (2008) 327–358. doi:10.1007/s11044-008-9123-5.

[23] S. Falomi, M. Malvezzi, E. Meli, Multibody modeling of railway vehicles: Innovative algorithms for the detection of wheel–rail contact points, Wear 271 (1-2) (2011) 453–461. doi:https://doi.org/10.1016/j.wear.2010.10.039.

[24] L. Baeza, D. J. Thompson, G. Squicciarini, F. D. Denia, Method for obtaining the wheel–rail contact location and its application to the normal problem calculation through 'CONTACT', Vehicle System Dynamics 56 (11) (2018) 1734–1746. doi:10.1080/00423114.2018.1439178.
[25] S. Muñoz, J. F. Aceituno, P. Urda, J. L. Escalona, Multibody model of railway vehicles with weakly coupled vertical and lateral dynamics, Mechanical Systems and Signal Processing 115 (2019) 570–592. doi:10.1016/j.ymssp.2018.06.019.
[26] J. L. Escalona, J. F. Aceituno, P. Urda, O. Balling, Railway multibody simulation with the knife-edge-equivalent wheel–rail constraint equations, Multibody System Dynamics (2019) 1–30doi:10.1007/s11044-019-09708-x.
[27] J. L. Escalona, J. F. Aceituno, Multibody simulation of railway vehicles with contact lookup tables, International Journal of Mechanical Science 155 (2019) 571–582. doi:https://doi.org/10.1016/j.ijmecsci.2018.01.020.
[28] M. Bozzone, E. Pennestrì, P. Salvini, A lookup table-based method for wheel–rail contact analysis, Proceedings of the Institution of Mechanical Engineers, Part K: Journal of Multi-body Dynamics 225 (2) (2011) 127–138.
[29] H. Sugiyama, K. Araki, Y. Suda, On-line and off-line wheel/rail contact algorithm in the analysis of multibody railroad vehicle systems, Journal of Mechanical Science and Technology 23 (2009) 991–996. doi:https://doi.org/10.1007/s12206-009-0327-2.
[30] H. Sugiyama, T. Sekiguchi, R. Matsumura, S. Yamashita, Y. Suda, Wheel/rail contact dynamics in turnout negotiations with combined nodal and non-conformal contact approach, Multibody System Dynamics 27 (2012) 55–74. doi:https://doi.org/10.1007/s11044-011-9252-0.
[31] J. Piotrowski, B. Liu, S. Bruni, The kalker book of tables for non-hertzian contact of wheel and rail, Vehicle System Dynamics 55 (6) (2017) 875–901.
[32] F. Marques, H. Magalhães, B. Liu, J. Pombo, P. Flores, J. Ambrósio, J. Piotrowski, S. Bruni, On the generation of enhanced lookup tables for wheel-rail contact models, Wear 434–435 (2019) 202993. doi:https://doi.org/10.1016/j.wear.2019.202993.
[33] J. Piotrowski, S. Bruni, B. Liu, E. D. Gialleonardo, A fast method for determination of creep forces in non-Hertzian contact of wheel and rail base on a book of tables, Multibody System Dynamics 45 (2019) 169–184. doi:https://doi.org/10.1007/s11044-018-09635-3.
[34] J. Santamaría, E. G. Vadillo, J. Gómez, A comprehensive method for the elastic calculation of the two-point wheel–rail contact, Vehicle System Dynamic 44 (sup1) (2006) 240–250. doi:https://doi.org/10.1080/00423110600870337.
[35] J. F. Aceituno, P. Urda, E. Briales, J. L. Escalona, Analysis of the two-point wheel-rail contact scenario using the knife-edge-equivalent contact constraint method, Mechanism and Machine Theory 148 (2020) 103803. doi:https://doi.org/10.1016/j.mechmachtheory.2020.103803.
[36] J. Kalker, Three dimensional elastic bodies in rolling contact, Kluwer Academic Publishers, Dordrecht/-Boston/London, 1990.
[37] O. Polach, Creep forces in simulations of traction vehicles running on adhesion limit, Wear 258 (7-8) (2005) 992–1000. doi:10.1016/j.wear.2004.03.046.
[38] K. Hunt, E. Crossley, Coefficient of restitution interpreted as damping in vibroimpact, Journal of Applied Mechanics 7 (1975) 440–445.
[39] A. A. Shabana, K. E. Zaazaa, H. Sugiyama, Railroad vehicle dynamics: a computational approach, CRC press, 2007.
[40] W. Goldsmith, Impact-the theory and physical pehaviour of colliding solids, Edward Arnold Ltd., London,England, 1960.
[41] U. M. Ascher, L. R. Petzold, Computer methods for ordinary differential equations and differential-algebraic equations, Vol. 61, Siam, 1998.
[42] O. Polach, A fast wheel-rail forces calculation computer code, Vehicle System Dynamics 33 (sup1) (1999) 728–739. doi:10.1080/00423114.1999.12063125.
[43] H. Claus, W. Schiehlen, Modeling and simulation of railway bogie structural vibrations, Vehicle System Dynamics 29 (1998) 538–552. doi:10.1080/00423119808969585.